Loss of contractile pericytes and their impaired calcium dynamics exacerbate brain ischemic stroke of awake mice in acute and chronic phases

Authors: *Lechan Tao[1], Chen He[1], Teddy Groves[2], Kayeon Kim[1], Krzysztof Kucharz[1], Aleksandra Petrovskaia [1], Dmitry Postnov[3], Xiao Zhang[1], Christina Latt Fjorbak[1], Henry Gordon Sansom[4], Hao Hu[4], Peter Andersen[4], Inge Mulder[5,6,7], Ed van Bavel[5,6,7], Anpan Han[8], Changsi Cai1[1†]*

Affiliations:

[1]Department of Neuroscience, Faculty of Health and Medical Science, University of Copenhagen, 2200, Copenhagen N, Denmark

[2]The Novo Nordisk Foundation Center for Biosustainability, Technical University of Denmark, Lyngby, 2800, Denmark

[3]Center of Functionally Integrative NeuroscienceDepartment of Clinical Medicine, Aarhus University, Aarhus, 8000, Denmark

[4]Department of Health Technology, Technical University of Denmark, 2800, Kongens Lyngby, Denmark

[5]Biomedical Engineering and Physics, Amsterdam University Medical Center, University of Amsterdam, Amsterdam, the Netherlands

[6]Amsterdam Neuroscience, Neurovascular Disorders, Amsterdam, the Netherlands

[7]Amsterdam Cardiovascular Sciences, Microcirculation, the Netherlands

[8]Department of Civil and Mechanical Engineering, Technical University of Denmark, Lyngby, 2800, Denmark

†Correspondence should be addressed to:

Changsi Cai, PhD.

Maersk Tower, 07.04.34

Blegdamsvej 3B, Copenhagen N

ccai@sund.ku.dk

Abstract

Ischemic stroke frequently results in persistent neurovascular uncoupling, whereby neuronal activity fails to evoke appropriate microvascular responses despite restoration of upstream blood flow. The cellular mechanisms governing this dysfunction along the arteriolar-capillary continuum remain poorly understood. Using two-photon microscopy and laser speckle imaging in awake Acta2-GCaMP8 mice subjected to transient middle cerebral artery occlusion, we examined calcium signaling and contractile function of vascular smooth muscle cells, precapillary sphincters (PS), and contractile pericytes during stroke progression. During acute phase, PSs exhibited pronounced calcium elevations and strong constriction, amplifying downstream capillary constriction through spatially localized calcium signaling. Following reperfusion, excessive calcium elevations persisted without proportional diameter changes, indicating calcium signaling dysregulation and early uncoupling between mural cell calcium dynamics and vascular responses. In the chronic phase, ischemia induced PS-associated loss of contractile pericytes, leading to capillary dilation and sustained impairment of neurovascular coupling. Although pericyte coverage and calcium signaling partially recovered from second week post stroke, whisker-evoked vascular responses and calcium sensitivity remained compromised. At the network level, blood flow responses became spatially heterogeneous, with pericyte-lost regions exhibiting prolonged hyporesponsiveness during functional hyperemia. These findings identify PSs as key regulators of ischemia-induced microvascular dysfunction and highlight mural cell calcium dysregulation and pericyte loss as drivers of persistent neurovascular uncoupling after stroke.

Key words: Ischemic stroke, neurovascular uncoupling, PSs, contractile pericytes, calcium signaling

Introduction

Ischemic stroke, characterized by the acute occlusion of a cerebral artery causing insufficient blood flow and tissue infarction, remains a leading cause of global disability and mortality[1]. However, even with successful recanalization of large vessels, persistent microvascular dysfunction, such as neurovascular uncoupling[2–4] and the 'no reflow'[5–8] phenomenon, continues to limit effective reperfusion and exacerbate brain injury within the ischemic penumbra.

Neurovascular coupling (NVC) refers to the regional regulation of cerebral blood flow in response to dynamic neuronal metabolic demands. Vascular mural cells are the only contractile element to change vessel diameters and blood flow, which includes vascular smooth muscle cells (VSMCs) on arteries and arterioles and contractile pericytes on the initial branches from arterioles to capillaries, pericytes at capillary bed and venules[9,10]. VSMCs on arteries and arterioles and contractile pericytes on the first few branches of capillaries have been reported to play a major role in blood flow regulation during NVC[11–13]. Furthermore, the conventional opinion that pericytes at capillary bed and venous are non-contractile have been challenged by a few recent studies, showing their containing of α-smooth muscle actin (α-SMA)[14], demonstrating slow and weaker regulation of NVC [15,16].

Pericytes are increasingly recognized as an important player in brain ischemic stroke. Previous studies have demonstrated that pericytes undergo dramatic contraction and 'die-in-rigor' during both occlusion and reperfusion phase[17], while prolonged contraction by pericytes at capillary bed during the chronic phase promote 'no flow' phenomena and exacerbate capillary stalling[18]. Despite these advances, how ischemia differentially affects VSMCs, contractile pericytes, and specialized microvascular control points within the ischemic penumbra across stroke progression remains poorly understood.

A key structure at this transition is the precapillary sphincter (PS), a specialized structure comprising VSMCs-pericyte-hybrid cells located at the arteriolar-capillary junction[19]. PS has recently been recognized as a critical gatekeeper for blood flow into downstream capillary beds, protecting downstream capillaries from pressure fluctuations. Although PSs share many vasoactive signaling pathways with VSMCs[20], PSs demonstrate superior responsiveness compared to VSMCs and contractile pericytes during NVC, capable of both strong dilation (~ 30-60%) and constriction (~ 80%)[19–21]. Notably, PSs exhibit heightened vulnerability to pathological events like cortical spreading depolarization and aging, exhibiting greater increases in flow resistance and desensitization of signaling by local puff of vasoactive compounds[19,22]. Despite their recognized physiological importance, the contribution of PSs to ischemia-induced microvascular dysfunction has not been systematically investigated.

Mural cells regulate vascular tone and contribute to rapid NVC responses, primarily via intracellular calcium (Ca^{2+}) signaling and actin–myosin light-chain–dependent contractile mechanisms[23,24]. Yet, comprehensive examination of functional Ca^{2+} dynamics of VSMCs, PSs, and contractile pericytes during stroke progression, in both acute and chronic phases, are lacking. Particularly, pericyte Ca^{2+} dynamics and vascular responsivity measured in the awake state are more physiologically relevant than measurements obtained under anesthesia; however,

in the context of ischemic stroke, these awake-state measures have not been reported previously. Given the unique contractile capabilities and regulatory function of PSs, as well as their potential to influence neighboring mural cells, their specific contribution to microvascular dysfunction, and neurovascular uncoupling phenomenon in stroke warrants dedicated investigation.

In this study, we aimed to characterize dynamic changes in Ca^{2+} signaling and contractility of VSMCs, PSs, and contractile pericytes during both the acute and chronic phases of experimental ischemic stroke. We hypothesized that post-ischemic Ca^{2+}-dependent hypercontractility in PSs disrupts adjacent mural cell function, impairs downstream capillary reperfusion, and exacerbates neurovascular uncoupling, contributing to poor outcome despite successful upstream vessel recanalization. Using two-photon microscopy (TPM), we investigated Ca^{2+} dynamics and corresponding capillary changes across these mural cell populations during stroke progression. Our results reveal that PSs play a pivotal role in stroke pathophysiology. In the acute phase, PS-adjacent contractile pericytes exhibit aberrantly elevated Ca^{2+} signaling accompanied with excessive capillary constriction, leading to chronic pericyte loss and capillary dilation, as well as impaired vascular reactivity. In contrast, non-PS-related contractile pericytes demonstrate greater survival and better preservation of vascular tone and NVC responses. Although pericyte coverage and Ca^{2+} signaling partially recovered at later stages, activity-evoked vascular responses and calcium sensitivity remained impaired, leading to spatially heterogeneous blood flow during functional hyperemia. Together, these findings identify PSs as vulnerable control points linking ischemic injury to persistent neurovascular uncoupling and microvascular dysfunction.

Results

Sharp calcium rise in mural cells, especially precapillary sphincters, induces strong capillary constriction during the acute phase of ischemic stroke

To investigate the effects of PSs during acute phase of ischemic stroke, we performed craniotomy and transient filament middle cerebral artery occlusion (MCAO) model on Acta2-GCaMP8 mice. Using *in vivo* two-photon microscopy (TPM), we recorded regions of interest (ROIs) encompassing mural cell calcium dynamics together with diameter changes in corresponding penetrating arterioles (PAs) and downstream capillaries. As described in methods, PSs were identified based on their anatomical location at the arteriolar–capillary junction, characteristic focal indentation in vessel diameter, and morphology of surrounding mural cells. PS locations were mapped within the cranial window, and ROIs with and without PSs were imaged at baseline, during occlusion, and 15 min after reperfusion. Further, we classified capillaries by their branching orders, with the first order being the first capillary branching from the PA, and so forth (**Fig. 1A, B, Supplemental Fig. 1**).

During occlusion, the calcium intensity in PSs increased by 58.94 ± 14.58%, which caused a 33.16 ± 4.699% reduction in vascular diameter (**Fig. 1C, E**). PAs and 1st -3rd order capillaries also exhibited significant constriction (**Fig. 1F, H**). However, in ROIs lacking PSs (non-sph group), capillaries showed markedly weaker constriction than those associated with PSs (sph group), particularly in downstream capillaries, whereas PAs constricted to a similar extent in

both groups (**Fig. 1F, H**). Notably, the calcium changes during occlusion did not significantly differ between sph and non-sph groups (**Fig. 1D, G**). Segment-specific analysis further revealed that in sph ROIs, PSs, adjacent PAs, and first-order capillaries exhibited stronger calcium increases than second- and third-order capillaries, whereas calcium elevations were relatively uniform across segments in non-sph ROIs (**Fig. 1G**). Together, these findings indicate that the presence of a PS amplifies downstream capillary constriction through spatially localized calcium signaling rather than changes in overall mural cell calcium magnitude.

After reperfusion, calcium intensity in PSs increased by 264.5 ± 42.31%, accompanied by a 47.4 ± 4.467% diameter reduction relative to baseline (**Fig. 1C, E**). In contrast to the occlusion phase, vessel diameters after reperfusion did not differ significantly between sph and non-sph groups **(Fig. 1F, H**). Capillaries downstream of PSs remained constricted at a level similar to that observed during occlusion, whereas capillaries in non-sph ROIs exhibited enhanced constriction after reperfusion, reaching a magnitude comparable to sph-associated capillaries (**Fig. 1F, H**). These findings suggest that capillaries downstream of PSs quickly reached near-maximal constriction during occlusion, whereas capillaries in non-sph ROIs constricted more gradually and only achieved comparable constriction after reperfusion. Despite the lack of further diameter reduction, calcium levels increased more sharply during reperfusion in all vessel segments of the sph group compared with the non-sph group (**Fig. 1D, G**), indicating dysregulation of calcium signaling, characterized by elevated intracellular calcium that no longer translated into proportional contractile responses. This exaggerated calcium rise diminished progressively in more distal capillaries, mirroring the spatial pattern observed during occlusion and suggesting that the presence of a PS is associated with early and pronounced calcium elevations in adjacent mural cells.

To quantify the relationship between calcium level and vascular diameter, we performed Pearson correlation analysis at different time points. During occlusion, calcium and diameter changes in PSs exhibited a strong negative correlation, consistent with calcium-dependent constriction; however, this relationship was disrupted following reperfusion (**Fig. 1I**). The pronounced calcium elevation during reperfusion without additional constriction suggests calcium dysregulation in mural cells. In first-order capillaries, calcium dynamics were uncoupled from diameter changes during both occlusion and reperfusion (**Fig. 1J**), indicating that ischemia-induced dysregulation of calcium-dependent contractile signaling in contractile pericytes begins during the occlusion phase. Together, these findings demonstrate a segment-specific disruption of calcium-dependent vascular control during the acute phase of ischemic stroke.

Sphincter-associated loss of contractile pericyte coverage post ischemic stroke

Abnormal intracellular calcium rise is highly cytotoxic, activating calpains that degrade cytoskeletal and organelle proteins and driving mitochondrial dysfunction through Ca^{2+} accumulation, loss of membrane potential, and caspase activation[25–27], potentially leading to cell death and structural remodeling after ischemia. Previous studies have demonstrated that while the initial wave of pericyte death occurs hyper-acutely, the maximum reduction in pericyte coverage and the peak of delayed cell death (including necroptosis) in the ischemic

penumbra are most pronounced between days 3 and 7[18,28,29]. After day 7, robust angiogenesis[28,30] and pericyte proliferation[29,31,32] typically observed. To investigate how PS-related microvascular impairments evolve post stroke, we thereby performed immunohistochemistry on mouse brains collected 4 days post-stroke. Mural cells were labeled by PDGFR-β, contractile pericytes, VSMCs and PSs were labeled using α-SMA, while vessels were labeled by podocaylxin.

To quantify contractile pericyte coverage, we measured the distance from PA-1st order capillary junction to the distal endpoint of contractile pericyte coverage (α-SMA-positive coverage), as well as the capillary order at the endpoint. In general, contractile pericyte coverage distance was significantly shorter on the ipsilateral side compared to the contralateral side (**Fig. 2A-C**). When further stratified by the presence of PSs, this reduction was significantly more pronounced in the sph group, whereas the non-sph group exhibited only a moderate decrease in coverage distance (**Fig. 2B, E**). Similarly, the capillary order at the endpoint of contractile pericyte coverage was lower on the ipsilateral side, particularly in vessels associated with PSs (**Fig. 2B, D, F**). When comparing sph and non-sph branches arising from the same PA, coverage distance was also significantly shorter in PS-associated branches on the ipsilateral side, but not on the contralateral side (**Fig. 2G**). These results suggest that ischemic stroke reduces contractile pericyte coverage, and this effect is exacerbated in the presence of a PS.

Longitudinal in vivo imaging reveals progressive loss of pericyte calcium signaling and capillary responsivity

Given the acute calcium surge in PS-associated regions and the reduction in contractile pericyte coverage revealed by immunohistochemistry, we hypothesized that PSs were associated with enhanced contractile pericyte loss and more severe mural cell dysfunction during the chronic phase after stroke. To test this, we performed longitudinal TPM and laser speckle imaging (LSI) in awake Acta2-GCaMP8 mice. Fast repetitive volumetric (x–y–z–t) hyperstack imaging was used to capture the full vascular architecture and dynamic mural cell activity over time. The main function of VSMCs, PSs and contractile pericytes are regulation of vascular tone during resting state and blood flow during hyperemia. We thereby recorded mural cell calcium signals and corresponding vascular diameters under resting condition and in response to whisker air puff stimulation (**Fig. 3A, B**).

Starting as early as one day post-stroke, we observed a progressive loss of detectable calcium signals, most prominently in contractile pericytes on first-order capillaries (**Fig. 3C-E**). Quantification across vessel segments and time points revealed that loss of pericyte calcium signals occurred predominantly in capillaries during the first week following ischemia (**Fig. 3C–E**). To objectively classify pericyte signal loss, we quantified calcium coverage relative to baseline (D0), as well as foreground-background contrast. ROIs not fulfilling all criteria were classified as preserved (**Supplemental Fig. 2**). Detailed criteria are described in the Method section. We calculated the proportion of preserved and unpreserved pericytes both in sph and non-sph groups. Strikingly, 67% of ROIs in the sph group exhibited unpreserved pericytes,

compared with only 25% in the non-sph group (**Fig. 3F**), indicating that the presence of a PS is strongly associated with post-stroke loss of contractile pericyte calcium signaling.

Loss of contractile pericytes can disrupt the basal tone regulation. To assess this, we measured resting-state vessel diameters across different vascular segments over time (**Supplemental Fig. 3A**). Significant dilation was observed at first- and second-order capillaries during the first two weeks after ischemia, whereas PAs and PSs showed no significant diameter changes for most of the recording period. When vessel diameter measurements were stratified by preserved and unpreserved pericyte groups (**Fig. 3G**), capillaries and PAs in the unpreserved group exhibited significant dilation post stroke, in comparison to the unchanged resting state diameters in the preserved group. This is consistent with previous studies showing a loss of basal tone in regions with laser ablated or age-related coverage loss of pericytes[33,34].Although a trend toward dilation was also observed in PSs within the unpreserved group, these changes did not reach statistical significance across most of time points. Collectively, these findings demonstrate that ischemic stroke induces PS-associated loss of contractile pericytes during the chronic phase, contributing to impaired basal tone regulation and concomitant capillary dilation.

Functional hyperemia is impaired by attenuated calcium dynamics and vessel diameter changes at contractile pericytes

Having demonstrated a reduction in contractile pericyte coverage and increase of resting state diameter during the chronic phase after ischemic stroke, we next examined whether their capacity to regulate blood flow is also functionally impaired. To address this question, we applied air puff–induced whisker stimulation to awake Acta2-GCaMP8 mice and recorded mural cell calcium dynamics together with vascular diameter changes (**Fig. 3A, B**). At baseline (D0), all vascular segments exhibited robust calcium responses that effectively drove vessel dilation in response to whisker stimulation. Following ischemic stroke, however, both calcium and vascular responses were markedly attenuated (**Supplemental Fig. 4; Fig. 4**).

Overall, calcium responses were strongly suppressed during the first week post-stroke, with the exception that reductions in negative calcium peak changes in PAs persisted up to day 28 (**Supplemental Fig. 4A, B**). To determine whether loss of contractile pericytes contributed to these changes, we compared calcium response amplitudes between preserved and unpreserved groups across post-stroke time points. Both groups exhibited pronounced reductions in mural cell calcium response peaks across all vascular segments during the first week (**Fig. 4A–C**). From the second week onward, calcium responses in the remaining mural cells surrounding capillaries and PSs largely recovered. With the exception of second-order capillaries, no significant differences in calcium response amplitudes were observed between preserved and unpreserved groups across vessel segments and time points.

In contrast to calcium signaling, vascular responses to whisker stimulation remained impaired for up to 21 days post-stroke, far outlasting the period of suppressed calcium responses (**Supplemental Fig. 4; Fig. 4D–F**). Notably, capillaries and PSs in the unpreserved group exhibited a greater and more prolonged reduction in dilation amplitude compared with the preserved group (**Fig. 4D–F**). These findings indicate that the sustained impairment of vascular

responses cannot be explained by reduced calcium signaling in surviving mural cells but rather reflect loss of functional contractile pericytes. Collectively, these results demonstrate that ischemia leads to a disproportionate and prolonged impairment of vascular responses during functional hyperemia, particularly in regions with contractile pericyte loss. Importantly, this deficit persists even after partial recovery of mural cell calcium signaling, indicating a sustained reduction in the functional contribution of contractile pericytes to blood flow regulation following ischemic stroke.

Ischemia caused uncoupling between mural cell calcium dynamics and diameter changes, as well as a reduction in calcium sensitivity

To explore the mismatch between calcium and vascular responses during whisker stimulation, we performed Pearson correlation analysis to assess if ischemia disrupts the coupling between mural cell calcium dynamics and vessel diameter changes. When investigating the relationship between mural cell Ca^{2+} dynamics and vessel behavior during functional hyperemia, a direct correlation is expected. Elevations in Ca^{2+} activate the contractile machinery via calmodulin and myosin light chain kinase, leading to crossbridge cycling and active force generation[24]. This force produces vessel wall motion that manifests as dilation or constriction. The rate of vessel diameter change, i.e. wall speed, was dominated by the concomitant change in mural cell Ca^{2+}. Therefore, we compared calcium signals to the rate of diameter change (dD/dt), which more directly reflects the dynamic mechanical response to Ca^{2+} transients.

Consistent with this model, the derivative of diameter responses during whisker stimulation showed a strong inverse correlation with calcium responses, whereas direct linear correlation between calcium and diameter changes was weak or absent (**Fig. 5A, B**). We next examined this relationship across different vessel segments and time points after stroke. Ischemic stroke uncoupled calcium signaling from vascular response, lasting from 1 day in PAs to up to 7 days in PSs and capillaries (**Supplemental Fig. 5A, B**). The slope of regression line, which reflects the sensitivity of diameter changes to calcium transients, further revealed a prolonged impairment in calcium sensitivities within contractile pericytes up to D28 (**Supplemental Fig. 5A, C**).

To determine whether pericyte loss contributed to this uncoupling, we further stratified the data based on the preservation or loss of pericyte calcium signals. In capillaries, both the correlation coefficient (*R* value) and the regression slope were reduced to a greater extent and for a longer duration in the unpreserved group (**Fig. 5C, D**). In contrast, in PAs and PSs, reductions in R value and slope were largely confined to the first week after stroke (**Fig. 5D**). These findings are consistent with our earlier observations (**Fig. 4**), indicating that calcium signaling in survival mural cells is insufficient to effectively regulate vascular diameter once contractile pericytes are lost. Collectively, these results demonstrate that ischemia induces a sustained uncoupling between mural cell calcium dynamics and vascular responses, together with a reduction in calcium sensitivity, particularly in capillary regions affected by contractile pericyte loss.

Recovery of pericyte coverage does not fully restore whisker-evoked vascular responses after ischemic stroke.

Previous studies have shown that pericytes can extend their processes to compensate for the loss of adjacent pericytes, leading to recovery of pericyte coverage within 21 days after ablation under physiological conditions[33,34]. Consistent with this, we observed that ROIs exhibiting loss of pericyte calcium signals during the first week after stroke showed partial recovery of pericyte coverage from the second week onward (**Fig. 6A**). To determine whether this structural recovery was accompanied by restoration of pericyte function, we classified ROIs into unpreserved and recovered phases based on longitudinal changes in pericyte coverage. Recovery was defined as regrowth of pericyte coverage to either at least 25% above the minimum coverage observed after stroke or to more than 50% of baseline (D0) coverage. (**Supplemental Fig. 2**).

During the recovered phase, basal vascular tone and mural cell calcium responses to whisker stimulation largely returned toward baseline levels (**Fig. 6B, C**). In contrast, whisker-evoked vascular dilation remained significantly impaired in PAs and capillaries (**Fig. 6B**). Consistent with this observation, correlation analysis between the derivative of vessel diameter and calcium signals revealed persistent impairment in first-order capillaries during the recovered phase (**Fig. 6D**), indicating sustained dysfunction in vascular segments that previously experienced pericyte loss. In comparison, PSs exhibited only minor changes in vascular tone and whisker-evoked responses (**Fig. 6B-D**), suggesting greater resilience of PSs to ischemic injury relative to contractile pericytes. Together, these findings demonstrate that although pericyte coverage and calcium signaling can partially recover after ischemic stroke, this structural and signaling recovery is insufficient to fully restore neurovascular coupling. Instead, ischemia induces a long-lasting uncoupling between mural cell calcium dynamics and vascular responses during functional hyperemia, particularly in regions that experienced contractile pericyte loss.

Pericyte loss led to regional ischemia during functional hyperemia

Pericyte loss contributes to the heterogeneity of vascular impairments. Capillary segments lacking pericytes exhibited a pronounced dilation during resting state, and more severe impairment of NVC during whisker stimulation (**Fig. 3C, G; Fig. 4D-F**). These findings indicate dysregulation of microvessels both in resting state and functional hyperemia. To directly assess how ischemia alters blood flow distribution at the network level, we performed LSI to measure cortical blood flow responses to whisker stimulation across the cranial window over the course of stroke progression. In the healthy state, approximately 90% of the imaged cortical area exhibited a robust and spatially widespread increase in blood flow following whisker stimulation (**Fig. 7A, B**). Following ischemic stroke, these responses were markedly attenuated, particularly during the first week post-stroke, as reflected by significant reductions in both response area and peak amplitude (**Fig. 7A–E**). Beginning at day 14 post-stroke, blood flow responses partially recovered; however, both the responsive area and response amplitude remained significantly reduced compared with the healthy state.

To determine whether local pericyte loss contributed to these heterogeneous blood flow responses, we mapped ROIs previously monitored by TPM onto LSI heatmaps using pial arteries as anatomical landmarks (**Fig. 7F**). Blood flow changes during whisker stimulation

were quantified within circular regions (50 μm diameter) centered on TPM-recorded ROIs. The region size is rationalized based on the estimated distance of 130 μm between two adjacent PAs in mouse cortex[35]. During the early post-stroke period (days 1–4), blood flow responses were similarly reduced in regions associated with preserved and unpreserved pericytes. In contrast, from day 7 onward, blood flow responses in regions associated with preserved pericytes showed partial recovery, whereas regions associated with unpreserved pericytes remained largely unresponsive to stimulation (**Fig. 7G**). These findings closely mirror the TPM results and indicate that loss of contractile pericytes disrupts local regulation of vessel diameter, leading to persistent impairment of stimulus-evoked blood flow in adjacent cortical regions. Collectively, the data demonstrate that ischemia induces a redistribution of blood flow during functional hyperemia, driven in part by spatially heterogeneous pericyte loss and the resulting failure of local neurovascular control.

Discussion

In this study, we investigated the role of Ca^{2+}-dependent contractility in mural cells, specifically SMCs, PSs, and contractile pericytes, across acute and chronic phases of ischemic stroke. Our results identify PSs as key regulators of microvascular perfusion during ischemia, with an excessive Ca^{2+} sensitivity and pathological contraction to ischemia and unique influence on adjacent contractile pericytes. We found that PS-adjacent contractile pericytes experienced severe Ca^{2+} increase and excessive vasoconstriction in the acute phase, leading to pericyte loss, and impaired ability to regulate vascular tone and responses in downstream capillary that persisted into the chronic phase. In contrast, non-PS-associated contractile pericytes exhibited more stable Ca^{2+} dynamics during acute phase, therefore better cell survival, and preserved vascular responses. Although pericyte coverage and calcium signaling partially recovered from second week post stroke, whisker-evoked vascular responses remained suppressed. This segment-specific disparity in mural cell behavior appears to contribute to neurovascular uncoupling, as well as the redistribution of perfusion.

While PSs have been previously identified as gatekeepers regulating capillary blood flow under physiological conditions[19], our study is the first to demonstrate their critical role during the progression of ischemic stroke. Earlier studies have shown that pericytes can contract capillaries during ischemia and hinder reperfusion[12,18], contributing to the no reflow after reperfusion. Our data reveal that PSs are more contractile and more susceptible to ischemic Ca^{2+} rise than other mural cells. The heightened Ca^{2+} influx in PS may arise from their strategic anatomical location at the arteriolar-capillary interface, their enriched expression of a-SMA, and their active role in blood flow regulation[13,19]. Functionally, PSs must integrate local metabolic signals to ensure appropriate perfusion of downstream capillaries. This dual regulatory role likely accounts for their great responsiveness compared to downstream pericytes. As a result, PSs exhibit pronounced contractile changes during both the acute drop in blood flow following occlusion and the subsequent surge during reperfusion (**Fig. 1B, C, E**). The observed calcium changes in pericytes adjacent to precapillary sphincters may result from intercellular communication through direct membrane contacts such as gap junctions, as well as endothelial-mediated transmission[36–39], allowing the propagation of Ca^{2+} signals along the vascular wall in response to sphincter activity. This mechanism is supported by our observation

that calcium transients in pericytes diminish with increasing distance from the sphincter during the acute phase, suggesting a spatially coordinated signaling process (**Fig. 1G**).

Consistent with previous studies[18,28,29], we observed pericyte loss during the chronic phase, which may result from excessive calcium increase occurring in the acute phase. Calcium overload is known to activate cytoplasmic calpain, leading to the degradation of cytoskeletal, endoplasmic reticulum, and mitochondrial proteins[40–42]. Additionally, excessive intracellular calcium can drive Ca^{2+} influx into mitochondria, elevating mitochondrial membrane potential, disrupting mitochondrial function, and triggering the caspase cascade, ultimately culminating in cell death [25–27]. Although we observed strong correlations between Ca^{2+} increase and cell loss, mechanisms require further validation using genetic or pharmacological manipulation of Ca^{2+} handling. Our acute-phase observations align with earlier reports[17,18,43,44] that pericytes contract post ischemia. However, unlike previous studies, we did not observe 'die in rigor' into the chronic phase. Instead, we found a marked and prolonged capillary dilation following pericyte coverage loss (**Fig. 3G**), likely due to the clearance of dead pericytes by glial cells and macrophages[45,46], leading to a loss of vascular tone regulation at those sites. These findings suggest that contractile pericyte contraction is a transient event limited to the acute phase of ischemia, while the chronic phase is characterized by capillary dilation resulting from the absence of contractile regulation due to contractile pericyte loss.

Interestingly, although SMCs, PSs, and contractile pericytes all exhibited excessive calcium elevations during the acute phase, it was primarily contractile pericytes, particularly those on 1st-order capillaries, that demonstrated a higher likelihood of pericyte coverage loss. Notably, PSs showed even greater calcium increases than pericytes (PSs: 264.5 ± 42.31; PAs: 260.9 ± 47.31; 1st-order capillaries: 201.9 ± 30.79; 2nd-order: 142.6 ± 22.78; 3rd-order: 107.7 ± 37.36) yet remained more structurally intact. Several factors may explain this paradox: 1. Higher baseline calcium levels in PSs and SMCs (**Fig. 1B**) may indicate an inherently greater tolerance to calcium overload. 2. Robust cellular morphology, including thicker cell bodies and more circumferential vessel coverage[19,20,22,47] (**Fig.2B; Fig.3C**), likely offers mechanical stability and resistance to ischemia compared to the thinner, sparser distributed pericytes. 3. The high expression of α-SMA in PSs and PAs (**Fig. 2B**) may help maintain cytoskeletal integrity under pathological conditions.

The resulting contractile pericyte loss leads to structural and functional remodeling of downstream capillaries, including chronic dilation and blunted reactivity, which collectively contribute to impaired perfusion adaptability during both baseline conditions and NVC responses (**Fig. 3; Fig. 4**). Neuronal loss has been reported post stroke[48,49]. It may partially lead to the overall reduction in calcium signaling and vascular responses observed in both regions with and without pericyte loss. However, when capillaries were stratified based on pericyte presence, those lacking pericyte exhibited more pronounced impairment in vascular reactivity, along with a decoupling between calcium dynamics and diameter changes. This spatially localized dysfunction is unlikely to be explained solely by impaired neuroglial signaling and instead suggests a direct consequence of pericyte loss. As a result, these injury-prone regions exhibit a failure to adequately recruit blood during functional hyperemia, further exacerbating neurovascular uncoupling and tissue hypoperfusion.

Moreover, the heterogeneity of pericyte dysfunction following ischemia disrupts the spatial and temporal coherence of capillary blood flow regulation. In areas where pericytes remain functional, blood flow can still be appropriately directed in response to neuronal activity. In contrast, regions with pericyte dysfunction experience delayed and weak responses, resulting in spatial displacement of blood flow recruitment during neuronal activation. This mismatch between perfusion and metabolic demand leads to further impaired functional hyperemia. Persistent NVC impairment can worsen the neurological outcome and slow functional recovery following stroke[3]. This differential vulnerability underscores the importance of considering microvascular heterogeneity in stroke pathophysiology.

Several limitations of this study should be acknowledged. First, while two-photon imaging provides high-resolution data on Ca^{2+} dynamics, our measurements are limited to cortical surface microvessels and may not fully capture deeper or regional heterogeneity. Second, although we observed strong correlations between Ca^{2+} overload, contractile behavior, and pericyte coverage loss, causal mechanisms require further validation using genetic or pharmacological manipulation of Ca^{2+} handling. Finally, our study was conducted in a rodent model of stroke, and future research is needed to confirm the relevance of these mechanisms in human tissue. Future studies should aim to dissect the upstream triggers of Ca^{2+} dysregulation in PSs, explore their interactions with endothelial and immune cells during stroke progression, and test therapeutic interventions that preserve PS function. It will also be important to determine whether PS dysfunction is reversible or represents a point of no return in stroke-induced microvascular damage.

In conclusion, our findings identify PSs as a functionally distinct and highly vulnerable microvascular component during ischemic stroke. Through their abnormal Ca^{2+}-dependent contractility and influence on surrounding mural cells, PSs contribute to impaired reperfusion, disrupted neurovascular coupling, and chronic capillary dysfunction. Targeting these mechanisms may offer a better recovery after traditional large-vessel recanalization approaches. Future studies will aim to dissect the upstream triggers of Ca^{2+} dysregulation in PSs, explore their interactions with endothelial and immune cells during stroke progression, and test therapeutic interventions that preserve PS function.

Method

1. Animal

Acta2-GCaMP8.1/mVermilion (Tg(Acta2-GCaMP8.1/mVermilion) B34-4Mik, JAX #032887; Jackson Laboratory) mice and C57BL/6J mice (Jackson Laboratory) of both sexes, aged 10 to 22 weeks, were used in this study (8 males and 10 females). All procedures were approved by the Danish National Committee on Health Research and conducted in accordance with the European Council's Convention for the Protection of Vertebrate Animals used for experimental and other scientific purposes, adhering to established animal research guidelines. All mice were maintained under a 12-hour light/dark cycle, with ad libitum access to food and water via the cage lid.

2. Chronic cranial window implantation

Mice were anesthetized with 1–2% isoflurane and placed in a stereotaxic frame on a temperature-controlled heating pad (37 °C), with body temperature continuously monitored via a rectal probe. Preoperative analgesia and anti-inflammatory treatment included subcutaneous carprofen (5 mg/kg), buprenorphine (0.05 mg/kg), dexamethasone (4.8 mg/kg), and 0.5 mL sterile saline; 0.1 mL Lidocaine was injected locally at the surgical site.

A cranial window (Ø ~4 mm) was drilled over the left hemisphere (anterior-posterior: -1.5 mm; medial-lateral: -3 mm), covered with a 5 mm glass coverslip, and secured using 3M™ RelyX™ resin cement. A lightweight stainless steel head plate (Neurotar®) was affixed to the skull using Paladur® dental cement, ensuring complete coverage with no exposed skull.

Postoperatively, mice received 0.5 mL sterile saline and were maintained on a heating pad overnight. Analgesia (carprofen and buprenorphine) continued for 3 days. Animals were monitored daily for 7 days, and experiments were performed ≥ 4 weeks after surgery.

3. Transient filament middle cerebral artery occlusion (MCAO)

Transient middle cerebral artery occlusion (MCAO) was performed as described by Longa et al.[50] Preoperative analgesia included subcutaneous carprofen (5 mg/kg), buprenorphine (0.05 mg/kg), and 0.5 mL sterile saline. Anesthesia and temperature control were identical to those used for cranial window surgery.

MCAO was induced by insertion of a filament and maintained for either 30 min (chronic experiments) or 60 min (acute experiments), depending on the experimental group. Sham-operated animals underwent identical surgical procedures without arterial occlusion. Successful occlusion was verified by laser Doppler flowmetry.

Neurological deficits were assessed using the extended Garcia neurological scoring system following transient MCAO, as described by Garcia et al.[51] Postoperative supportive care, including daily subcutaneous administration of carprofen, buprenorphine, and saline, was provided for three days to minimize mortality. Body weight and general behavior were monitored daily during the first postoperative week.

4. In vivo imaging during acute phase of ischemic stroke

Acta2-GCaMP8.1/mVermilion transgenic mice were anaesthetized with 1% isoflurane and body temperature was maintained as described in Section 2. To visualize the vasculature, 50 µL of 2% (wt/vol) Texas Red-dextran (70 kDa, Invitrogen) was administered via retro-orbital injection prior to imaging.

Imaging was performed using a commercial two-photon microscope (FluoView FVMPE-RS, Olympus). Epifluorescence images of the entire craniotomy were acquired using a 4×, 0.16 NA air objective and a scientific CMOS camera (ORCA-Flash 2.8, Hamamatsu). Capillary segments, including sphincter-associated and non-sphincter regions, were mapped using a 25×, 1.05 NA water-immersion objective and identified on epifluorescence angiograms (**Supplemental Fig. 1**).

Mural cell calcium dynamics and vascular diameters were acquired based on these angiograms using volumetric 4D (x–y–z–t) hyperstack imaging with the 25×, 1.05 NA objective, covering vascular segments from PAs to second- or third-order capillaries. Image stacks were acquired at a spatial resolution of 0.118–0.495 µm/pixel (512 × 512 pixels), with a z-step of 2.0–2.58 µm, comprising 11–27 planes per stack, at a scan speed of 2.0 µs/pixel (~15 s per stack). Each ROI was recorded for six imaging cycles and averaged for analysis.

For ROIs containing precapillary sphincters, high-resolution volumetric imaging was performed. These stacks were acquired at 0.026-0.062 µm/pixel (1024 × 1024 pixels), with a z-step of 1.5 µm, comprising 6-17 planes per stack, at 2.0 µs/pixel (15-32 s per stack). Each ROI was recorded for three cycles and averaged.

Excitation wavelength was set to 920 nm. Emitted fluorescence from GCaMP8.1 (VSMCs and pericytes) was collected using a band-pass filter of 489-531 nm, while Texas Red–dextran signals (vessel lumens) were collected using a 601-657 nm band-pass filter. Identical laser parameters were used for calcium signal acquisition across all imaging time points.

5. Longitudinal two-photon Imaging

Longitudinal imaging was performed using a commercial two-photon microscope (Femto3D-RC, Femtonics) equipped with a 25×, 1.0 NA piezo-driven objective and controlled by Femtonics MES v6 software. Recordings were conducted at days 0, 1, 4, 7, 14, and ≥21 post-surgery (**Fig. 3A, B**).

Fast repetitive hyperstack imaging (4D imaging) was performed for each ROI (**Fig. 3B**), covering segments from PAs to second-order capillaries. This approach enabled the visualization of entire z-axis ranges of the targeted vessels at desired spatial and temporal resolution. Each image stack was acquired in under 1 second and consisted of 6–11 planes with a step size 3.5–5.5 µm. Pixel size in the x–y plane ranged from 0.33 to 0.57 µm/ pixel. Excitation was provided at 920 nm, and emitted fluorescence was spectrally separated to capture green signals from GCaMP8.1-expressing Acta2-positive mural cells and red signals from Texas Red–dextran–labeled vessel lumens.

For awake imaging, whisker air-puff stimulation was delivered during hyperstack acquisition, following a baseline period of at least 30 s and 60s post stimulation. Air-puff stimulation (1 s duration at 3 Hz, 0.25 s pulse width) was applied to the distal whiskers via a metal tube. Facial behaviors (pupillometry and whisking) and body behaviors (locomotion and grooming) were monitored using two synchronized cameras. Real-time locomotion speed was recorded using the integrated Neurotar Mobile HomeCage magnetic tracking system, which computes cage position and velocity from magnetic sensors independent of lighting conditions (**Fig. 3B**). Pupil size, whisking, and locomotion were recorded simultaneously with two-photon imaging.

Trials exhibiting movement artifacts (locomotion speed >1 cm/s or overt limb activity such as grooming or lifting) were excluded from analysis. Only motion-free trials were included in whisker-evoked response analyses, and spontaneous movement periods were excluded from resting-state measurements. For each mouse, data were collected from three ROIs.

6. Laser speckle contrast imaging

Cortical cerebral blood flow (CBF) was measured using LSI in awake Acta2-GCaMP8 mice immediately following TPM at days 0, 1, 4, 7, 14, and ≥21 post-surgery (**Fig. 2A**). The recording setup was customized as previously described[52]. Illumination was provided by a volume holographic grating–stabilized laser diode (LP785-SAV50, Thorlabs) controlled by a CLD1011LP driver (Thorlabs). Images were acquired using a CMOS camera (acA2040-90umNIR, Basler) coupled to a 5× objective (0.15 NA; HCX PL FLUOTAR, Leica), yielding a spatial resolution of 3.19 µm/pixel (1024 × 1024 pixels) at 50 frames per second.

Awake imaging procedures followed those described in Method Section 5. CBF responses to whisker stimulation (1 s at 3 Hz, 0.25 s pulse duration) were recorded for 90 s, including a 30 s baseline and 60 s post-stimulation period. Animal behavior was continuously monitored using synchronized video cameras and a locomotion sensor.

To minimize stress, total recording time per mouse per session was limited to 1.5 h (1.25 h TPM and 15 min LSI). Sessions were terminated early if signs of distress were observed. LSI data were processed offline using custom-written code in MATLAB (R2021b)[53].

7. Identification of precapillary sphincters

As described in a previous study[19], the precapillary sphincter is defined as a mural cell encircling an indentation of the capillary at the point where it branches from a PA. In this study, precapillary sphincters were identified based on the following three criteria: (1) Location: situated at the junction between the PA and a first-order capillary; (2) Diameter: the indentation at the junction was < 0.8× the diameter of the first-order capillary; and (3) Morphology: the indentation was encircled by a thick mural cell (GCaMP8.1 expression). Only regions fulfilling all three criteria were classified as precapillary sphincters.

8. Pericyte coverage loss identification and classification

For longitudinal analyses, each pericyte ROI was tracked across time and classified according to its signal state and fate. Pericyte calcium signals were analyzed within predefined vascular ROIs using ImageJ/Fiji on calibrated images. All preprocessing steps were kept identical across time points within each mouse.

Pericyte signal detection was performed within each ROI using ImageJ's Auto Threshold function. The thresholding method (Default, Triangle, Moments, or Li) was selected for each ROI based on baseline (D0) segmentation quality and then kept constant for that ROI across all time points. Thresholds were applied only within the ROI to avoid bias from unrelated bright structures.

High-threshold coverage (Coverage%) was defined as the fraction of ROI pixels above the selected threshold. d. To determine whether apparent coverage loss reflected true signal disappearance rather than poor signal-to-noise ratio or residual weak fluorescence, the mean intensity of suprathreshold pixels ($mean_{high}$) and subthreshold pixels ($mean_{low}$) within each ROI

were quantified. Background mean (μ_{bg}) and standard deviation (σ_{bg}) were measured from a fixed parenchymal background ROI for each mouse and used to compute Z-scores:

$$Z_{low} = \frac{mean_{low} - \mu_{bg}}{\sigma_{bg}}, \quad Z_{high} = \frac{mean_{high} - \mu_{bg}}{\sigma_{bg}}$$

ROIs were classified into two states: unpreserved or preserved pericytes. An ROI was classified as unpreserved if all the following criteria were met:

1. Reduced calcium coverage: high-threshold coverage < 50% of baseline (D0).
2. Loss of local signal: mean intensity at the coverage-reduced site < $\mu_{bg} + 3\times \sigma_{bg}$ (subthreshold signal indistinguishable from background; $Z_{low} < 3$).
3. Adequate signal-to-noise: mean intensity of maintained regions > $\mu_{bg} + 4\times\sigma_{bg}$ ($Z_{high} > 4$), ensuring sufficient imaging quality.
4. Vascular dilation: vessel diameter at the coverage-reduced site increased by > 20% relative to pre-stroke baseline.

Classification required confirmation at least two consecutive imaging sessions or at the terminal time point. ROIs not fulfilling all criteria were classified as preserved. This combined structural (coverage and diameter) and intensity-based approach ensured robust discrimination between true pericyte signal loss and changes arising from weak fluorescence or reduced imaging quality. This criterion ensured that apparent reductions in pericyte coverage reflected true signal loss rather than weak fluorescence, reduced imaging quality, or threshold-dependent segmentation artifacts.

9. Two-photon imaging analysis

All data were processed using ImageJ/Fiji or custom-written scripts developed in MATLAB (R2021b).

Analysis of data in acute phase of stroke

During the acute phase, vessel diameters and mural cell calcium intensities were quantified from two-photon images generated by mean intensity projection using ImageJ/Fiji. Vessel diameters were measured by placing multiple linear ROIs perpendicular to the vessel lumen and averaging multiple measurements across ROIs at each capillary order. For calcium signal analysis, ROIs were drawn along the morphological boundaries of mural cells at different vascular segments. Default thresholding method was applied to delineate GCaMP8.1-labeled mural cells in the image by mean intensity projection across the whole video, and only pixels above threshold were included in the analysis. ROIs were placed at identical locations and in the same number across time points, using mural cell morphology as a reference.

Whisker air puff stimulation analysis in chronic phase of stroke

For fast repetitive hyperstack imaging during whisker stimulation, image stacks were first motion-corrected and then collapsed along the z-axis using average-intensity projection to generate a time series of projected images (x–y–t), which was used for all subsequent analyses. Vascular diameter responses were quantified from the projected image series using a custom

MATLAB algorithm as described before[22,52]. Rectangular ROIs (2–4 μm wide) were placed perpendicular to the vessel axis at predefined locations. Vessel boundaries were detected over time using a Chan–Vese active contour segmentation algorithm, and diameter changes were extracted accordingly.

Calcium responses to whisker stimulation were quantified from the same projected image series using ImageJ/Fiji, following the protocol used for acute-phase analysis. ROIs were placed at identical locations and in the same number across time points, using mural cell morphology as a reference.

Correlation analysis between diameter and calcium

To assess the coupling between vascular diameter changes and calcium dynamics at different stages following ischemic stroke, the temporal derivative of the vessel diameter response was computed and tested linear correlation with the corresponding calcium signal. Pearson correlation coefficients and slope of regression lines were calculated to quantify the relationship between the two measures. All correlation analyses were performed using custom MATLAB scripts (R2021b), with statistical significance defined as $P < 0.05$.

10. Brain collection

C57BL/6J mice underwent MCAO surgery and postoperative care as described in Section 3, with an occlusion duration of 30 minutes. Four days after surgery, mice were anesthetized and transcardially perfused with saline for 3 minutes, followed by 4% paraformaldehyde (PFA) in 0.1 M PBS for 2 minutes. Brains were extracted and post-fixed in 4% PFA at 4 °C for 2 hours, then transferred to 30% sucrose at 4 °C for 48 hours. Samples were subsequently frozen in dry ice–chilled isopentane and stored at approximately –80 °C until use.

11. Immunohistochemistry and confocal imaging

Brains were sectioned coronally at 50 μm thickness using a cryostat. Sections were rinsed in phosphate-buffered saline (PBS) for 5 minutes, three times. Permeabilization and blocking were performed overnight at 4 °C in PBS containing 1% bovine serum albumin (BSA) and 0.5% Triton X-100. Sections were then incubated at 4°C for two nights with the following primary antibody: rat anti podocalyxin (1:400, MAB1556, R&D Systems), goat anti-PDGFRb (1:250, AF1042, R&D Systems), mouse anti-α-SMA-FITC (1:200, F3777, MilliporeSigma). After three 5-minute PBS washes, sections were incubated overnight at 4°C with secondary antibodies: donkey anti-goat IgG H&L (Alexa Fluor 647) (1:500, A-11057, Invitrogen), donkey anti-rat IgG H&L (Alexa Fluor 647) (1:500, A78947, Invitrogen). Following three additional 5-minute PBS washes, sections were stained with Hoechst 33342 (1:6000, B2261, Sigma) for 7 minutes. After a final series of three PBS washes, sections were mounted using SlowFade Diamond antifade mountant (Invitrogen, S36963) and sealed with nail polish.

Stained sections were scanned using Zeiss Axioscan 7 with a 20× objective at a resolution of approximately 0.172 μm/pixel (x and y) and 3 μm (z-step) for whole-slice overview imaging. High-resolution images were acquired using a Zeiss LSM 980 confocal microscope equipped with a 40× water-immersion objective.

Image analysis was performed by FiJi (US National Institutes of Health). The distance from penetrating arterioles (PAs) to the endpoint of contractile pericyte coverage, as well as the capillary branch order at the endpoint, were quantified based on αSMA (marking smooth muscle cells and contractile pericytes) and podocalyxin (marking vessels) expression.

12. Statistical analysis

Frequentist statistical analyses were performed using GraphPad Prism8, and Bayesian statistical analyses were implemented in Python using custom-written code.

Frequentist statistical analyses

Data are presented as mean ± s.e.m., with individual data points shown. For statistical analyses, values from individual ROIs were averaged per mouse. Paired *t*-tests were used for comparisons between two paired groups. One-way ANOVA was applied for comparisons involving more than two groups with a single factor, and mixed-effects models were used for analyses involving multiple groups measured at two or three time points. Post hoc multiple-comparison tests with appropriate correction were applied where indicated. All statistical tests were two-sided. Statistical significance was defined as * $P < 0.05$, ** $P < 0.01$, *** $P < 0.001$, and **** $P < 0.0001$.

Bayesian statistical analyses

Bayesian state space analysis of time-dependent vascular changes

For data comprising multiple groups measured across more than three time points (**Fig. 3G; Fig. 4C, F; Fig. 5D; Fig. 7C–E, G; Supplemental Fig. 3; Supplemental Fig. 4B, D; Supplemental Fig. 5B, C**), a Bayesian state space modelling approach was used to account for temporal dependence between repeated measurements. This framework allows estimation of time-varying effects while accommodating measurement noise and irregular sampling intervals. The overall statistical approach follows a recently published study that applied Bayesian multilevel analyses to microvascular dynamics[21].

For each ROI, measurements were collected at multiple time points. Temporal changes relative to baseline (D0) were quantified as relative changes from y_0 (data at D0, before MCAO surgery):

$$r_t = \frac{y_t - y_0}{y_0}$$

For measurements in which baseline normalization could lead to instability (e.g., when baseline values were near zero or could take both positive and negative values), absolute changes $(y_t - y_0)$ were used instead for statistical analysis. Graphs shown in the figures display the original values of $(y_t - y_0) / y_0$. To facilitate prior specification and improve numerical stability, all outcomes were standardized within each dataset prior to modelling.

General temporal dynamics (**Supplemental Fig. 3; Supplemental Fig. 4B, D; Supplemental Fig. 5B, C**) were modelled using a Gaussian random walk prior, corresponding to a discrete-time state space model. The latent standardized response $\hat{r}_t^{std}$ evolved as:

$$\hat{r}_1^{\text{std}} \sim \mathcal{N}(0,1)$$
$$\hat{r}_t^{\text{std}} \sim \mathcal{N}\left(\hat{r}_{t-1}^{\text{std}}, \tau\sqrt{\delta_t}\right), t > 1$$

where $\delta_t$denotes the time interval between consecutive observations and τ is a volatility parameter controlling temporal variability. This formulation explicitly encodes temporal dependence while allowing gradual, data-driven deviations over time.

To assess post-stroke outcome associated with the presence of pericyte (**Fig. 3G; Fig. 4C, F; Fig. 5D; Fig. 7C–E**), an additional time-varying parameter $\alpha_t^p$was included for affected measurements. This parameter was also modelled using a Gaussian random walk prior with its own volatility parameter τ^p:

$$\alpha_1^p \sim \mathcal{N}(0,1),$$
$$\alpha_t^p \sim \mathcal{N}\left(\alpha_{t-1}^p, \tau^p \cdot \sqrt{\delta^t}\right), t > 1.$$

Observed measurements were modelled using a Gaussian distribution to accommodate occasional outliers:

$$r_t^{\text{std}} \sim \begin{cases} \mathrm{N}(\hat{r}_t^{\text{std}}, \sigma), & \text{preserved,} \\ \mathrm{N}(\alpha_t^p, \sigma), & \text{unpreserved.} \end{cases}$$

Weakly informative priors were used for all hyperparameters, promoting model identifiability while avoiding overfitting. Posterior inference was performed using adaptive Hamiltonian Monte Carlo sampling with the Python library pymc[54]. Model convergence was assessed using standard diagnostics, including improved $\hat{R}$ convergence statistic[55], effective sample sizes, and the absence of post-warmup divergent transitions. Model adequacy was evaluated via posterior predictive checks, ensuring consistency between observed data and model-generated predictions.

Statistical conclusions were based on posterior distributions rather than null hypothesis significance testing. For each time point, we calculated the posterior probability that the estimated effect differed from baseline (D0). Effects were considered present when more than 95% of posterior samples shared the same sign. Instructions for reproducing our analysis are available at a GitHub repository (https://github.com/teddygroves/stroke/).

<u>Bayesian analysis of capillary order measurements from immunochemistry</u>

Capillary order at the endpoint of αSMA transition was analyzed using a Bayesian ordinal regression model, as capillary order is a discrete, ordered variable (values 1–6). This approach preserves ordinal structure without assuming continuity or equal spacing between categories. Capillary order was modelled as a function of capillary type (sphincter vs. non-sphincter), anatomical site (ipsilateral vs. contralateral), their interaction, and a random intercept to account for repeated measurements within individual mice:

$$order \sim capillary\ type + site + capillary\ type{:}\,site + (1 \mid mouse).$$

The model was implemented and fitted using Markov chain Monte Carlo sampling with the Python library Bambi[56], using weakly informative prior distributions. Model convergence and sampling quality were assessed using standard diagnostics.

Statistical inference was based on posterior distributions. For each comparison, we calculated the posterior proportion that one condition exceeded the other. Comparisons for which this proportion exceeded 0.95 (or was below 0.05) were interpreted as showing strong evidence for a directional effect. Instructions for reproducing our analysis are available at a GitHub repository (https://github.com/teddygroves/stroke/).

Acknowledgement

C.C acknowledges support from the Lundbeck Foundation (#R345-2020-1440, #R436-2023-1125, #R392-2018-2266, and #R345-2020-1440), the Independent Research Fund Denmark (#1133-00016B and #1030-00374A), the Novo Nordisk Foundation (#0064289, #0092323, #117272, #14CC0001), Læge Sofus Carl Emil Friis og Hustru Olga Doris Friis' Legat, Dagmar Marshalls Fond, Familien Hede Nielsens Fond, Hørslev fonden, Oda og Hans Svenningsens Fond, and Helsefonden. We used AI language tools for grammar checking and language refinement during manuscript preparation. Some images were created using Biorender.com under license.

References

1. Feske SK. Ischemic stroke. *Am J Med*. 2021;134(12):1457-1464.

2. He F, Sullender CT, Zhu H, et al. Multimodal mapping of neural activity and cerebral blood flow reveals long-lasting neurovascular dissociations after small-scale strokes. *Sci Adv*. 2020;6(21):eaba1933. doi:10.1126/sciadv.aba1933

3. Staehr C, Giblin JT, Gutiérrez-Jiménez E, et al. Neurovascular Uncoupling Is Linked to Microcirculatory Dysfunction in Regions Outside the Ischemic Core Following Ischemic Stroke. *J Am Heart Assoc*. 2023;12(11):e029527. doi:10.1161/JAHA.123.029527

4. Povlsen GK, Longden TA, Bonev AD, Hill-Eubanks DC, Nelson MT. Uncoupling of neurovascular communication after transient global cerebral ischemia is caused by impaired parenchymal smooth muscle Kir channel function. *Journal of Cerebral Blood Flow & Metabolism*. 2016;36(7):1195-1201. doi:10.1177/0271678X16638350

5. El Amki M, Glück C, Binder N, et al. Neutrophils obstructing brain capillaries are a major cause of no-reflow in ischemic stroke. *Cell Rep*. 2020;33(2).

6. Soares BP, Tong E, Hom J, et al. Reperfusion is a more accurate predictor of follow-up infarct volume than recanalization: a proof of concept using CT in acute ischemic stroke patients. *Stroke*. 2010;41(1):e34-e40.

7. Ames 3rd A, Wright RL, Kowada M, Thurston JM, Majno G. Cerebral ischemia. II. The no-reflow phenomenon. *Am J Pathol*. 1968;52(2):437.

8. Allencherril J, Jneid H, Atar D, et al. Pathophysiology, diagnosis, and management of the no-reflow phenomenon. *Cardiovasc Drugs Ther*. 2019;33(5):589-597.

9. Lind BL, Kucharz K, Cai C. In vivo two-photon microscopy for studies of neurovascular coupling in rodents: a beginner's guide. *Neurophotonics*. 2025;12(S2):S22808-S22808.

10. Grant RI, Hartmann DA, Underly RG, Berthiaume AA, Bhat NR, Shih AY. Organizational hierarchy and structural diversity of microvascular pericytes in adult mouse cortex. *Journal of Cerebral Blood Flow & Metabolism*. 2019;39(3):411-425.

11. Gonzales AL, Klug NR, Moshkforoush A, et al. Contractile pericytes determine the direction of blood flow at capillary junctions. *Proceedings of the National Academy of Sciences*. 2020;117(43):27022-27033.

12. Hall CN, Reynell C, Gesslein B, et al. Capillary pericytes regulate cerebral blood flow in health and disease. *Nature*. 2014;508(7494):55-60.

13. Zambach SA, Cai C, Helms HCC, et al. Precapillary sphincters and pericytes at first-order capillaries as key regulators for brain capillary perfusion. *Proceedings of the National Academy of Sciences*. 2021;118(26):e2023749118.

14. Alarcon-Martinez L, Yilmaz-Ozcan S, Yemisci M, et al. Capillary pericytes express α-smooth muscle actin, which requires prevention of filamentous-actin depolymerization for detection. *Elife*. 2018;7:e34861.

15. Hartmann DA, Berthiaume AA, Grant RI, et al. Brain capillary pericytes exert a substantial but slow influence on blood flow. *Nat Neurosci*. 2021;24(5):633-645.

16. Rungta RL, Chaigneau E, Osmanski BF, Charpak S. Vascular compartmentalization of functional hyperemia from the synapse to the pia. *Neuron*. 2018;99(2):362-375.

17. Hall CN, Reynell C, Gesslein B, et al. Capillary pericytes regulate cerebral blood flow in health and disease. *Nature*. 2014;508(7494):55-60. doi:10.1038/nature13165

18. Shrouder JJ, Calandra GM, Filser S, et al. Continued dysfunction of capillary pericytes promotes no-reflow after experimental stroke in vivo. *Brain*. 2024;147(3):1057-1074.

19. Grubb S, Cai C, Hald BO, et al. Precapillary sphincters maintain perfusion in the cerebral cortex. *Nat Commun*. 2020;11(1):395.

20. Zambach SA, Cai C, Helms HCC, et al. Precapillary sphincters and pericytes at first-order capillaries as key regulators for brain capillary perfusion. *Proceedings of the National Academy of Sciences*. 2021;118(26):e2023749118.

21. Fjorbak CL, Kutuzov NP, Groves T, Lauritzen M, Grubb S. Brain precapillary sphincters modulate myogenic tone in adult and aged mice. *Geroscience*. Published online 2025:1-20.

22. Cai C, Zambach SA, Grubb S, et al. Impaired dynamics of precapillary sphincters and pericytes at first-order capillaries predict reduced neurovascular function in the aging mouse brain. *Nat Aging*. 2023;3(2):173-184.

23. Korte N, Ilkan Z, Pearson CL, et al. The Ca 2+-gated channel TMEM16A amplifies capillary pericyte contraction and reduces cerebral blood flow after ischemia. *J Clin Invest*. 2022;132(9).

24. Hamilton NB, Attwell D, Hall CN. Pericyte-mediated regulation of capillary diameter: a component of neurovascular coupling in health and disease. *Front Neuroenergetics*. 2010;2:1453.

25. Bano D, Ankarcrona M. Beyond the critical point: an overview of excitotoxicity, calcium overload and the downstream consequences. *Neurosci Lett*. 2018;663:79-85.

26. Li YW, Liu Y, Luo SZ, et al. The significance of calcium ions in cerebral ischemia-reperfusion injury: mechanisms and intervention strategies. *Front Mol Biosci*. 2025;12:1585758.

27. Dhaouadi N, Vitto VAM, Pinton P, Galluzzi L, Marchi S. Ca2+ signaling and cell death. *Cell Calcium*. 2023;113:102759. doi:https://doi.org/10.1016/j.ceca.2023.102759

28. Fernández-Klett F, Potas JR, Hilpert D, et al. Early loss of pericytes and perivascular stromal cell-induced scar formation after stroke. *Journal of Cerebral Blood Flow & Metabolism*. 2013;33(3):428-439.

29. Xu Y, Chen C, Weng J, et al. Microcirculation Dysfunction in Subacute Stroke: The Role of Delayed Capillary Pericyte Loss. *Aging Dis*.

30. Ding G, Jiang Q, Li L, et al. Angiogenesis detected after embolic stroke in rat brain using magnetic resonance T2* WI. *Stroke*. 2008;39(5):1563-1568.

31. Shibahara T, Nakamura K, Wakisaka Y, et al. PDGFR β-positive cell-mediated post-stroke remodeling of fibronectin and laminin α 2 for tissue repair and functional recovery. *Journal of Cerebral Blood Flow & Metabolism*. 2023;43(4):518-530.

32. Shibahara T, Ago T, Tachibana M, et al. Reciprocal interaction between pericytes and macrophage in poststroke tissue repair and functional recovery. *Stroke*. 2020;51(10):3095-3106.

33. Berthiaume AA, Schmid F, Stamenkovic S, et al. Pericyte remodeling is deficient in the aged brain and contributes to impaired capillary flow and structure. *Nat Commun*. 2022;13(1):5912.

34. Berthiaume AA, Grant RI, McDowell KP, et al. Dynamic remodeling of pericytes in vivo maintains capillary coverage in the adult mouse brain. *Cell Rep*. 2018;22(1):8-16.

35. Nishimura N, Schaffer CB, Friedman B, Lyden PD, Kleinfeld D. Penetrating arterioles are a bottleneck in the perfusion of neocortex. *Proceedings of the National Academy of Sciences*. 2007;104(1):365-370.

36. Longden TA, Dabertrand F, Koide M, et al. Capillary K+-sensing initiates retrograde hyperpolarization to increase local cerebral blood flow. *Nat Neurosci*. 2017;20(5):717-726.

37. Hartmann DA, Coelho-Santos V, Shih AY. Pericyte control of blood flow across microvascular zones in the central nervous system. *Annu Rev Physiol*. 2022;84:331-354.

38. Hariharan A, Robertson CD, Garcia DCG, Longden TA. Brain capillary pericytes are metabolic sentinels that control blood flow through a KATP channel-dependent energy switch. *Cell Rep*. 2022;41(13).

39. Isaacs D, Xiang L, Hariharan A, Longden TA. KATP channel–dependent electrical signaling links capillary pericytes to arterioles during neurovascular coupling. *Proceedings of the National Academy of Sciences*. 2024;121(50):e2405965121.

40. Vindis C, Elbaz M, Escargueil-Blanc I, et al. Two distinct calcium-dependent mitochondrial pathways are involved in oxidized LDL-induced apoptosis. *Arterioscler Thromb Vasc Biol*. 2005;25(3):639-645.

41. Neuhof C, Neuhof H. Calpain system and its involvement in myocardial ischemia and reperfusion injury. *World J Cardiol*. 2014;6(7):638.

42. Zhang M, Wang G, Peng T. Calpain-mediated mitochondrial damage: an emerging mechanism contributing to cardiac disease. *Cells*. 2021;10(8):2024.

43. Qiu B, Zhao Z, Wang N, et al. A systematic observation of vasodynamics from different segments along the cerebral vasculature in the penumbra zone of awake mice following cerebral ischemia and recanalization. *Journal of Cerebral Blood Flow & Metabolism*. 2023;43(5):665-679.

44. Zhang S, Liao XJ, Wang J, et al. Temporal alterations in pericytes at the acute phase of ischemia/reperfusion in the mouse brain. *Neural Regen Res*. 2022;17(10):2247-2252.

45. Gardiner TA, Stitt AW. Juxtavascular microglia scavenge dying pericytes and vascular smooth muscle cells in diabetic retinopathy. *International Journal of Translational Medicine*. 2022;2(1):41-50.

46. Lapenna A, De Palma M, Lewis CE. Perivascular macrophages in health and disease. *Nat Rev Immunol*. 2018;18(11):689-702.

47. Grubb S. Ultrastructure of precapillary sphincters and the neurovascular unit. *Vascular Biology*. 2023;5(1).

48. Tuo Q, Zhang S, Lei P. Mechanisms of neuronal cell death in ischemic stroke and their therapeutic implications. *Med Res Rev*. 2022;42(1):259-305.

49. Mao R, Zong N, Hu Y, Chen Y, Xu Y. Neuronal death mechanisms and therapeutic strategy in ischemic stroke. *Neurosci Bull*. 2022;38(10):1229-1247.

50. Longa EZ, Weinstein PR, Carlson S, Cummins R. Reversible middle cerebral artery occlusion without craniectomy in rats. *Stroke*. 1989;20(1):84-91.

51. Garcia JH, Wagner S, Liu KF, Hu X jiang. Neurological deficit and extent of neuronal necrosis attributable to middle cerebral artery occlusion in rats: statistical validation. *Stroke*. 1995;26(4):627-635.

52. Zhang X, Tao L, Nygaard AH, et al. Aging alters calcium signaling in vascular mural cells and drives remodeling of neurovascular coupling in the awake brain. *Journal of Cerebral Blood Flow & Metabolism*. Published online 2025:0271678X251320455.

53. Boas DA, Dunn AK. Laser speckle contrast imaging in biomedical optics. *J Biomed Opt*. 2010;15(1):11109.

54. Abril-Pla O, Andreani V, Carroll C, et al. PyMC: a modern, and comprehensive probabilistic programming framework in Python. *PeerJ Comput Sci*. 2023;9:e1516.

55. Vehtari A, Gelman A, Simpson D, Carpenter B, Bürkner PC. Rank-normalization, folding, and localization: An improved R^for assessing convergence of MCMC (with discussion). *Bayesian Anal*. 2021;16(2):667-718.

56. Capretto T, Piho C, Kumar R, Westfall J, Yarkoni T, Martin OA. Bambi: A simple interface for fitting Bayesian linear models in Python. *J Stat Softw*. 2022;103:1-29.

Figure legends

Figure 1. Ischemic stroke induces robust calcium elevation in mural cells and pronounced constriction of PAs and capillaries.

(A) Experimental timeline of acute phase recording (top), schematic of the TPM imaging strategy (bottom left), and representative images illustrating ROIs with precapillary sphincters (PS; sph group) and without sphincters (non-sph group) (bottom right; scale bar, 50 μm). PAs, 1st-3rd order capillaries, and their associated mural cells were acquired as z-stacks using TPM.

(B) Representative imaging of non-sph (top row) and sph groups (middle row) at baseline, occlusion, and following reperfusion. Each ROI covers PA, 1st-3rd order capillaries (scale bar: 20 μm). PSs are further shown in the magnified imaging (bottom row, scale bar: 5 μm). Red: Texas Red–dextran (vessels); green: GCaMP8 fluorescence in Acta2-positive mural cells (VSMCs, PSs, and contractile pericytes).

(C, E) Calcium intensity (C) and diameter (E) changes in PSs across experimental time points (n = 10-12 ROIs from 5 mice).

(D, F) Calcium intensity (D) and diameter (F) changes in PAs, 1st - 3rd order capillaries, at different time points (n = 6-30 ROIs from 5 mice).

(G, H) Comparison of calcium signals (G) and diameter changes (H) between sph and non-sph groups during occlusion and reperfusion across different vascular segments (n = 6-30 ROIs from 5 mice).

(I, J) Scatter plot showing the relationship between calcium and diameter changes during occlusion and reperfusion in PSs (I; n = 10-11 ROIs from 5 mice), and 1st order capillaries (J; n = 9-17 ROIs from 5 mice). Light orange: occlusion; dark orange: reperfusion. Grey: preserved group; pink: unpreserved group.

All panels include data from n = 5 mice. Data are presented as mean ± SEM. Statistical analyses included one-way ANOVA for panels C and E, mixed-effects model for panels D, F, G, and H, and Pearson correlation analysis for panels I and J. Comparisons between baseline and post-stroke time points are indicated by # $P < 0.05$, ## $P < 0.01$, ### $P < 0.001$, #### $P < 0.0001$. All other comparisons are indicated by *$P < 0.05$, **$P < 0.01$, ***$P < 0.001$, **** $P < 0.0001$.

Figure 2. Ischemia-induced loss of contractile pericytes at day 4 post-stroke, analyzed by immunohistochemistry.

(A) Overview of the coronal brain section showing the contralateral (left) and ipsilateral (right) hemispheres, labeled with α-SMA (green), PDGFR-β (red), and podocalyxin (blue). Magnified images show representative regions from the contralateral (left), peri-infarct (middle), and ischemic core (right) areas (scale bar: 50 μm). Arrows indicate regions exhibiting loss of contractile pericytes.

(B) Representative images of vessels with and without PSs in contralateral and ipsilateral hemispheres (scale bar: 50 μm). Arrows denote the endpoints of contractile pericyte coverage, and arrowheads indicate the location of PSs.

(C, D) Quantification of the distance from the junction of the PA and the first-order capillary to the endpoint of contractile pericyte coverage (C), as well as the branch order at this endpoint (D), comparing vessel segments from contralateral and ipsilateral sides (n = 184-202 ROIs from 5 mice).

(E, F) Comparison of coverage distance (E) and branch order at endpoint (F) between capillaries with PSs (sph group) and those without PSs (non-sph group) (n = 57-127 ROIs from 5 mice).
(G) Representative images of vessel pairs with and without PSs arising from the same PA, along with quantitative comparison of coverage distances in contralateral and ipsilateral hemispheres (n = 12-16 vessel pairs from 5 mice).
Data are presented as mean ± SEM. Statistical analyses included paired t-test for panels C, Bayesian analysis for panels D and F, and mixed-effects model for panels E and G. Statistical significance in panels C, E, and G: * $P < 0.05$, ** $P < 0.01$. For panels D and F, * denotes a statistically supported conclusion with posterior probability (SP) > 0.95.

Figure 3. Long-term *in vivo* imaging reveals loss of pericyte calcium signaling accompanied by progressive capillary dilation following ischemic stroke.
(A) Experimental timeline for chronic-phase awake imaging in Acta2-GCaMP8 mice after ischemic stroke.
(B) Schematic of awake TPM imaging (left), imaging strategy (middle), and representative changes in vascular diameter and calcium intensity during resting state and whisker responses (right). Fluctuations during the resting state and responses evoked by whisker stimulation in vessels and mural cells were recorded using an x-y-z-t hyperstack. Z-projected signals across time were then quantified to generate diameter and calcium response curves during resting and stimulation periods.
(C) Representative images of ROIs showing preserved and unpreserved pericyte calcium signals at various days post-stroke (Scale bar: 20 µm). The red channel shows Texas Red-dextran-labeled vasculature, and the green channel shows GCaMP8 fluorescence. The magnified image highlights 1st order capillaries (Scale bar: 10 µm). (D) Percentage of unpreserved contractile pericytes across different vessel segments (N = 8 mice).
(E) Incidence of unpreserved pericytes (left) and percentage of mice exhibiting unpreserved pericytes (right) at different post-stroke time points (N = 8 mice).
(F) Percentage of vessels with maintained pericyte calcium signals (preserved group) and lost pericyte calcium signals (unpreserved group) in sph and non-sph groups.
(G) Comparison of percentage changes in vessel diameter over time between preserved and unpreserved groups across PAs, PSs, and first- and second-order capillaries (N = 8 mice).
Data are presented as mean ± SEM. Bayesian state-space analysis was applied for panel G. * indicates a statistically supported conclusion (SP > 0.95) for comparisons between preserved and unpreserved groups, whereas # denotes a statistically supported conclusion (SP > 0.95) for comparisons between baseline and post-stroke time points.

Figure 4. Ischemia reduces mural cell calcium and vascular responses to whisker stimulation.
(A, D) Representative images of whisker stimulation-induced mural cell calcium (A) and vascular (D) responses in ROIs with preserved and unpreserved pericyte calcium signals at D0 and D4 post-stroke (scale bar: 20 µm). Red: Texas Red–dextran; green: GCaMP8 fluorescence. Arrowheads indicate sites with absent calcium signals.

(B) Calcium response curves in mural cells from the corresponding vessel segments at D0 and at different post-stroke time points. Each curve represents the mean response overlaid from eight mice, with post-stroke days indicated by color.
(C) Amplitude of negative (top) and positive (bottom) calcium peaks in PAs, PSs, and 1st- (1stCap) and 2nd-order (2ndCap) capillaries at D1, D4, D7, D14, and ≥ D21 post-stroke, normalized to baseline (D0) (N = 8 mice).
(E) Percentage change in vascular response to whisker stimulation in PA, PSs, 1st and 2nd order capillaries at D0 and at subsequent post-stroke time points. Each curve represents the mean response overlaid from eight mice, with days indicated by color.
(F) Amplitude of peak vascular responses in PAs, PSs, and 1st- and 2nd-order capillaries at D1, D4, D7, D14, and ≥ D21 post-stroke, normalized to baseline (D0) (N = 8 mice).
Data are presented as mean ± SEM. Bayesian state-space analysis was applied for panels C and F. * indicates a statistically supported conclusion (SP > 0.95) for comparisons between preserved and unpreserved groups, whereas # denotes a statistically supported conclusion (SP > 0.95) for comparisons between baseline and post-stroke time points.

Figure 5. Ischemia induces uncoupling between calcium dynamics and vascular responses.
(A) Representative traces of whisker stimulation-induced vascular diameter changes (red), mural cell calcium responses (green), and the derivative of vascular diameter (purple) over time.
(B) Scatter plots showing the relationship between calcium signals and vascular diameter changes (right), as well as between calcium signals and the time derivative of diameter changes (left). Pearson correlation coefficients (*R*), *P* values, and slopes of the linear regression lines are indicated.
(C) Regression lines of calcium–vascular response correlations from 8 mice in preserved and unpreserved groups in 1st-order capillaries at D0 and D21. Green and brown lines indicate statistically significant correlations ($P < 0.05$), whereas red lines indicate non-significant correlations ($P \geq 0.05$).
(D) Summary of Pearson correlation coefficients (*R*; top) and slopes of regression lines (bottom) for correlations between calcium signals and the derivative of vascular diameter in PAs, PSs, 1st and 2nd order capillaries at D0 and various days post stroke (N = 8 mice).
Data are presented as mean ± SEM. Bayesian state-space analysis was applied for panel D. * indicates a statistically supported conclusion (SP > 0.95) for comparisons between preserved and unpreserved groups, whereas # denotes a statistically supported conclusion (SP > 0.95) for comparisons between baseline and post-stroke time points.

Figure 6. Recovery of pericyte coverage does not fully restore whisker-evoked vascular responses after ischemic stroke.
(A) Representative image of ROIs showing pericyte loss and subsequent regrowth at baseline (D0), D4 (unpreserved pericyte phase), and D21 (pericyte regrowth phase). Red: Texas Red–dextran; green: GCaMP8 fluorescence. Arrowheads indicate sites of absent and restored calcium signals. Scale bar: 20 μm.

(B, C) Basal diameter changes, amplitude of peak vascular responses (B) and mural cell calcium responses (C) in PA, PSs, 1st- and 2nd-order capillaries during the unpreserved and recovered phases (n = 6-45 ROIs from 8 mice).
(D) Pearson correlation coefficients (*R*) between calcium signals and the derivative of vascular diameter, as well as slopes of regression lines across vascular segments during the unpreserved and regrowth phases (n = 4-12 ROIs from 8 mice).
Data are presented as mean ± SEM. Paired t-test was applied for panels B-D. *$P < 0.05$, **$P < 0.01$, ***$P < 0.001$.

Figure 7. Regions associated with unpreserved pericytes exhibit a more severe impairment of whisker-evoked blood flow responses following ischemic stroke.
(A) Representative heatmaps showing changes in blood flow index (BFI) measured 5 s after air-puff–induced whisker stimulation at D0, D1, D4, D7, and D14 post-stroke. BFI values were calculated as the difference between post-stimulation and pre-stimulation (baseline) signals.
(B) Overlaid BFI response curves across different time points, with each day indicated by a distinct color. Each curve is the mean response overlaid from 6 mice.
(C, D) Raw peak amplitudes (C) and normalized peak amplitudes (D) of BFI responses evoked by whisker stimulation (N = 6 mice).
(E) Percentage of the responsive area relative to the total field of view at each time point (N = 6 mice).
(F) Top row: Average heatmaps of BFI changes at D0, D1, D4, D7, and D14, calculated over 2–4 s after whisker stimulation (scale bar, 1 mm). Hollow circles (ROI3) and dashed circles (ROI1, ROI2) indicate preserved and unpreserved pericyte–associated regions, respectively. Middle row: BFI response traces from preserved regions (green line, ROI3) and unpreserved pericyte–associated regions (brown dashed lines, ROI1 and ROI2) during whisker stimulation across post-stroke time points. Bottom row: Representative TPM images showing pericyte coverage in ROI1–ROI3 at D0 and D7.
(G) Comparison of raw and normalized peak BFI amplitudes evoked by whisker stimulation between preserved and unpreserved pericyte–associated regions across post-stroke time points (N = 6 mice).
Data are presented as mean ± SEM. Mixed-effects model was applied for panels C-E. Bayesian state-space analysis was applied for panel G. Statistical significance in panels C-E: * $P < 0.05$, ** $P < 0.01$, ***$P < 0.001$. For panel G, * denotes a statistically supported conclusion with posterior probability (SP) > 0.95.

Figure1

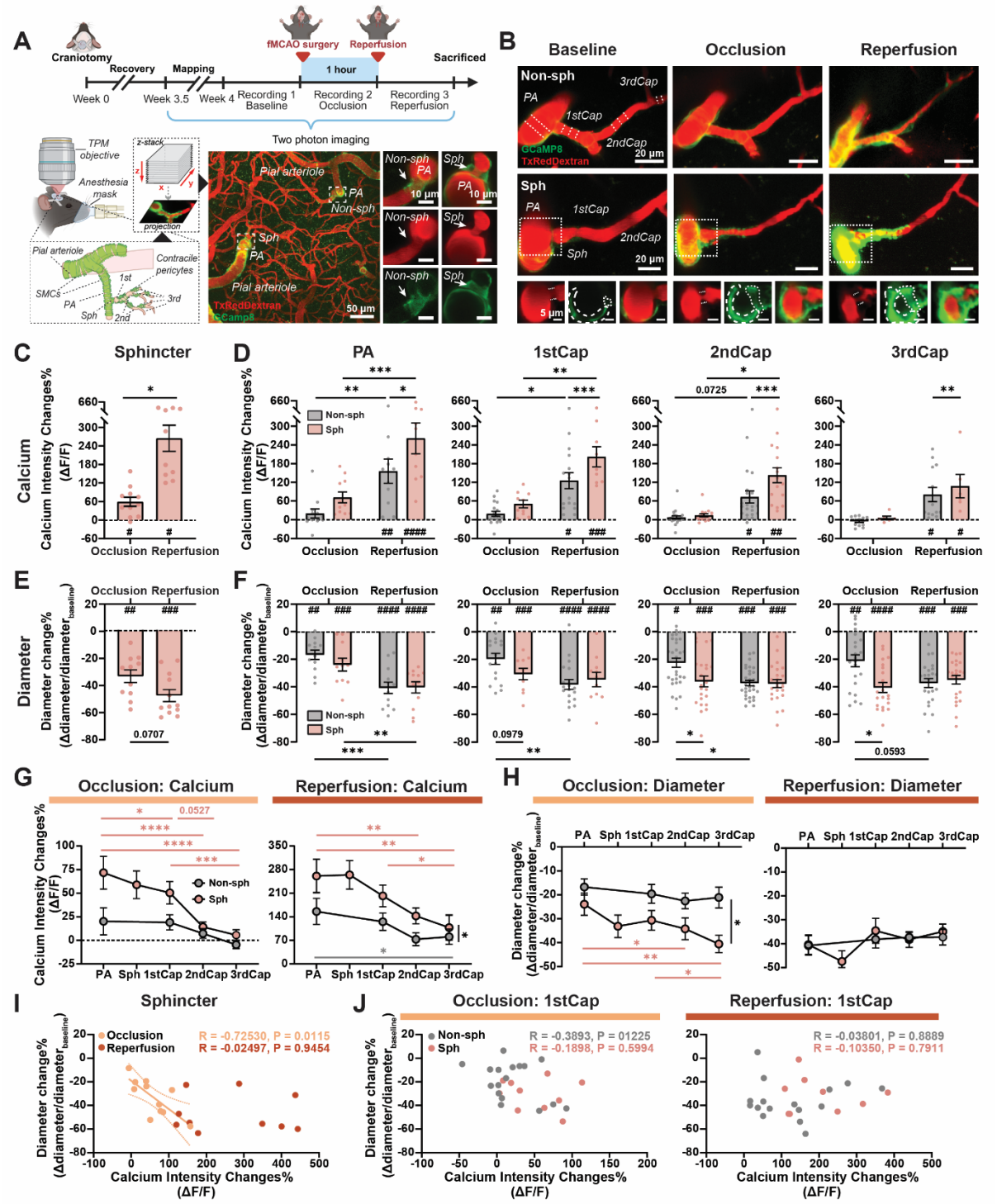
A
Craniotomy
Recovery
Mapping
fMCAO surgery
Reperfusion
1 hour
Sacrificed
Week 0
Week 3.5
Week 4
Recording 1 Baseline
Recording 2 Occlusion
Recording 3 Reperfusion
Two photon imaging
TPM objective
Anesthesia mask
z-stack
projection
Pial arteriole
Contracile pericytes
SMCs
PA
Sph
1st
2nd
3rd
Non-sph
TxRedDextran
GCamP8
50 μm
10 μm
B
Baseline
Occlusion
Reperfusion
Non-sph
3rdCap
1stCap
2ndCap
20 μm
5 μm
C
Sphincter
Calcium
Calcium Intensity Changes% (ΔF/F)
Occlusion
Reperfusion
D
PA
1stCap
2ndCap
3rdCap
Non-sph
Sph
E
Diameter
Diameter change% (Δdiameter/diameter baseline)
F
G
Occlusion: Calcium
Reperfusion: Calcium
H
Occlusion: Diameter
Reperfusion: Diameter
I
Sphincter
Occlusion
Reperfusion
R = -0.72530, P = 0.0115
R = -0.02497, P = 0.9454
Calcium Intensity Changes% (ΔF/F)
J
Occlusion: 1stCap
Reperfusion: 1stCap
R = -0.3893, P = 01225
R = -0.1898, P = 0.5994
R = -0.03801, P = 0.8889
R = -0.10350, P = 0.7911

Figure2

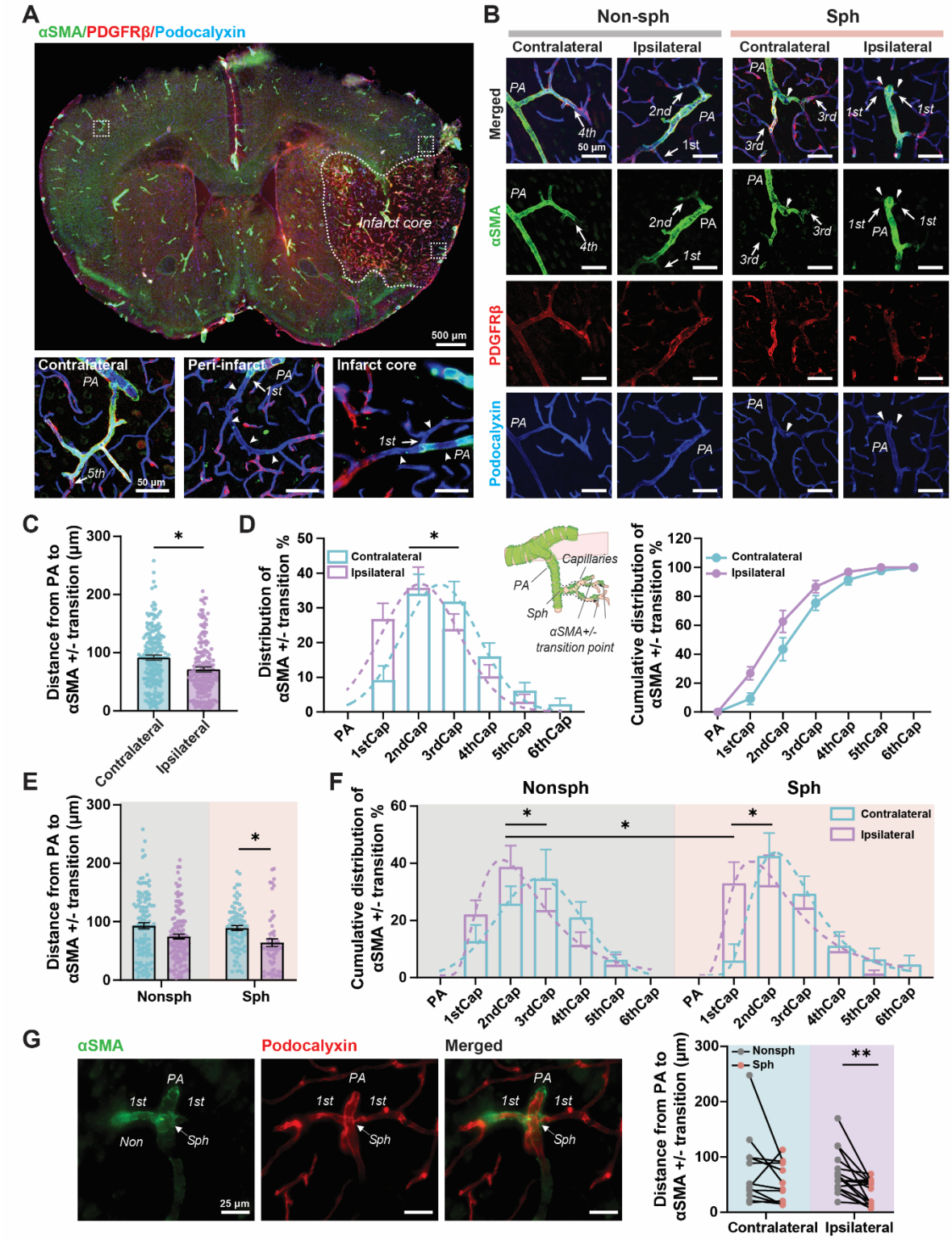
A
αSMA/PDGFRβ/Podocalyxin
Infarct core
500 μm
Contralateral
Peri-infarct
Infarct core
PA
1st
5th
50 μm
B
Non-sph
Sph
Contralateral
Ipsilateral
Merged
αSMA
PDGFRβ
Podocalyxin
PA
4th
2nd
3rd
1st
50 μm
C
Distance from PA to αSMA +/- transition (μm)
Contralateral
Ipsilateral
D
Distribution of αSMA +/- transition %
Capillaries
Sph
αSMA+/- transition point
PA
1stCap
2ndCap
3rdCap
4thCap
5thCap
6thCap
Cumulative distribution of αSMA +/- transition %
E
Nonsph
Sph
F
Nonsph
Sph
G
αSMA
Podocalyxin
Merged
Non
25 μm
Nonsph
Sph
Contralateral
Ipsilateral

Figure3

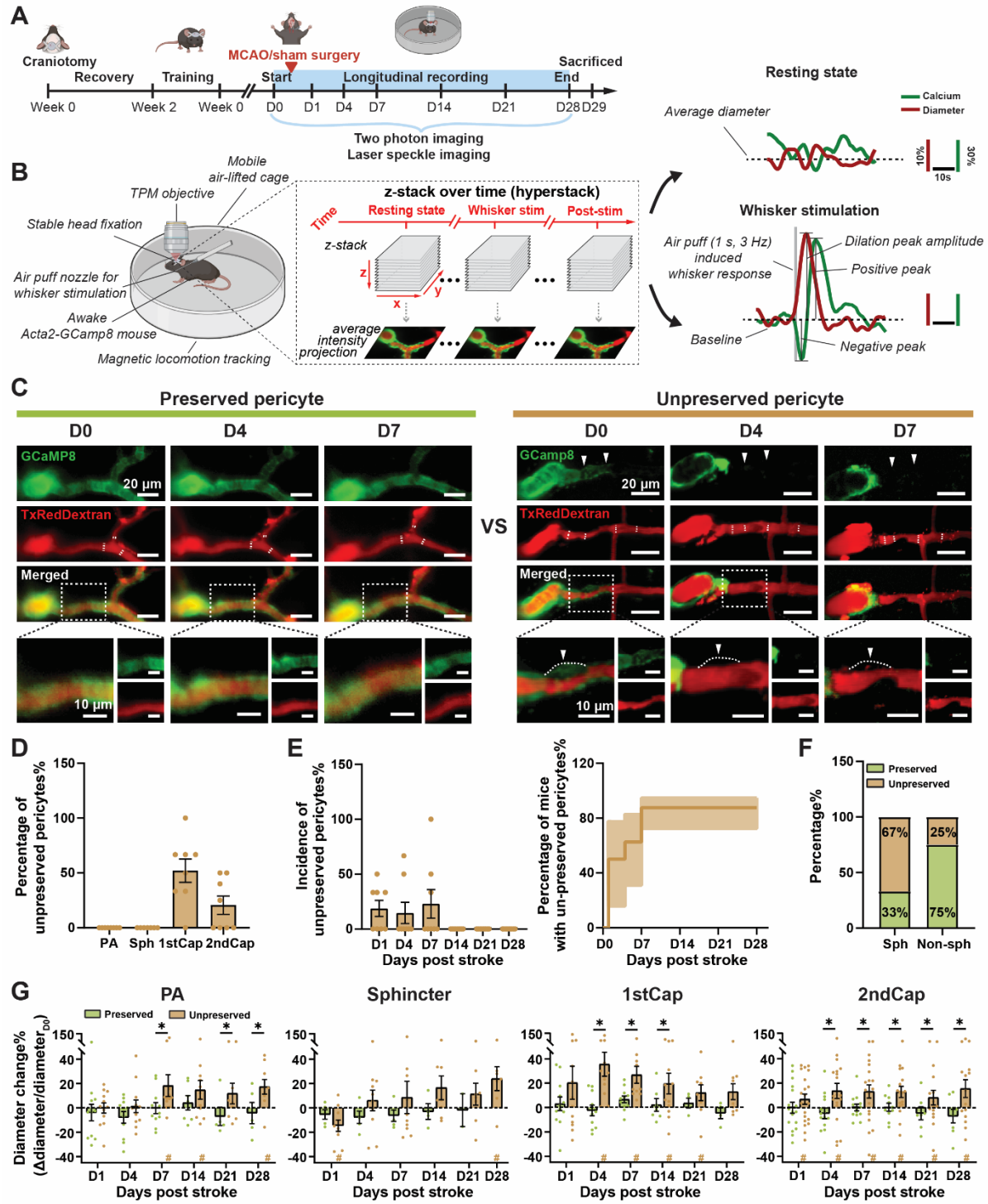
A
Craniotomy
Recovery
Training
MCAO/sham surgery
Start
Longitudinal recording
Sacrificed
End
Week 0
Week 2
Week 0
D0
D1
D4
D7
D14
D21
D28
D29
Two photon imaging
Laser speckle imaging
B
Mobile air-lifted cage
TPM objective
Stable head fixation
Air puff nozzle for whisker stimulation
Awake Acta2-GCamp8 mouse
Magnetic locomotion tracking
z-stack over time (hyperstack)
Time
Resting state
Whisker stim
Post-stim
z-stack
average intensity projection
Resting state
Average diameter
Calcium
Diameter
10%
30%
10s
Whisker stimulation
Air puff (1 s, 3 Hz) induced whisker response
Dilation peak amplitude
Positive peak
Baseline
Negative peak
C
Preserved pericyte
Unpreserved pericyte
D0
D4
D7
GCaMP8
GCamp8
TxRedDextran
Merged
20 μm
10 μm
VS
D
Percentage of unpreserved pericytes%
PA
Sph
1stCap
2ndCap
E
Incidence of unpreserved pericytes%
Days post stroke
Percentage of mice with un-preserved pericytes%
F
Preserved
Unpreserved
Percentage%
67%
33%
25%
75%
Sph
Non-sph
G
PA
Sphincter
1stCap
2ndCap
Diameter change% (Δdiameter/diameter$_{D0}$)
Days post stroke

Figure4

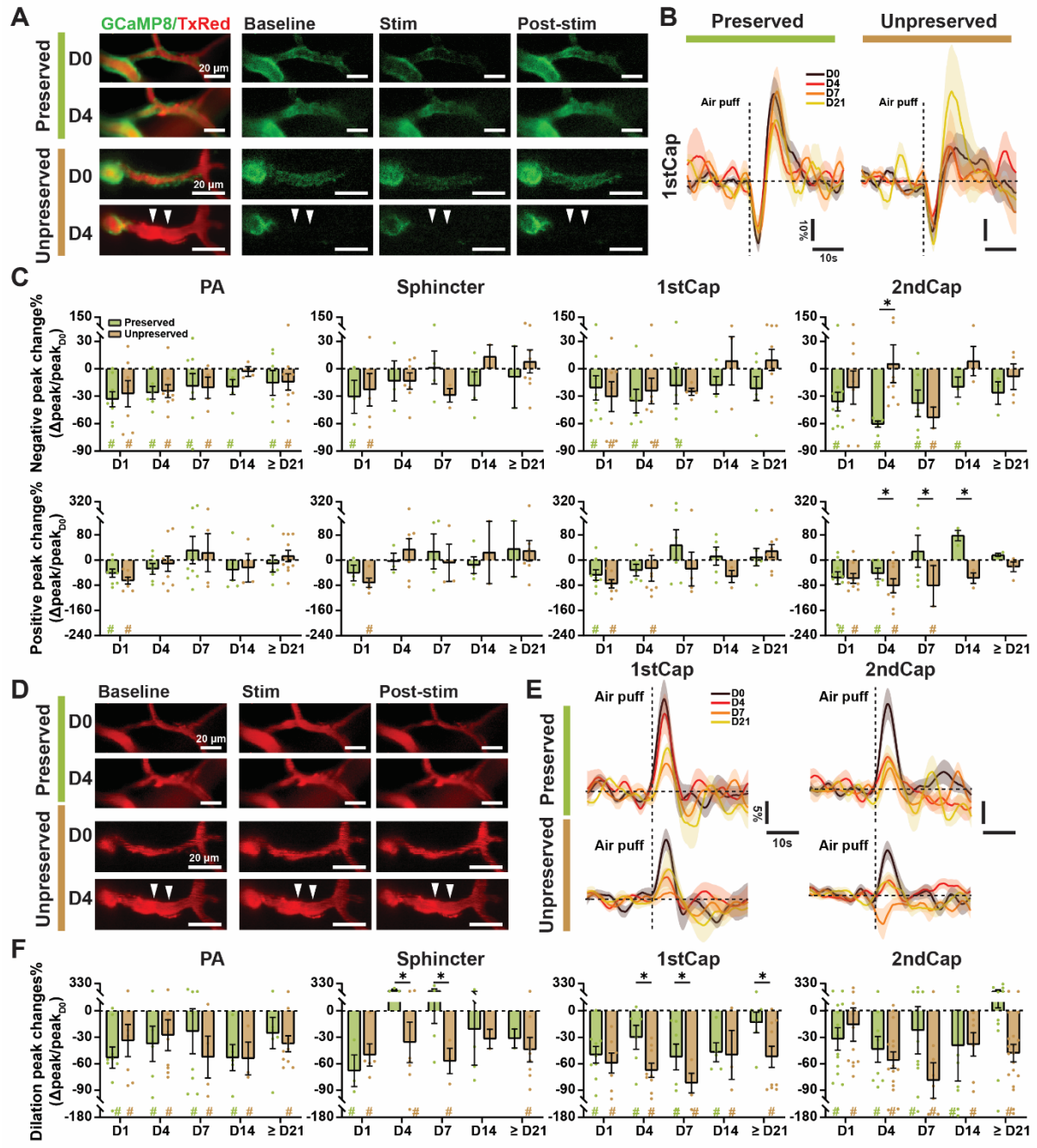
A
GCaMP8/TxRed
Baseline
Stim
Post-stim
Preserved
Unpreserved
D0
D4
20 μm
B
Preserved
Unpreserved
Air puff
D0
D4
D7
D21
1stCap
10%
10s
C
PA
Sphincter
1stCap
2ndCap
Preserved
Unpreserved
Negative peak change%
(Δpeak/peakD0)
Positive peak change%
(Δpeak/peakD0)
D1
D4
D7
D14
≥ D21
D
Baseline
Stim
Post-stim
E
1stCap
2ndCap
5%
10s
F
Dilation peak changes%
(Δpeak/peakD0)

Figure5

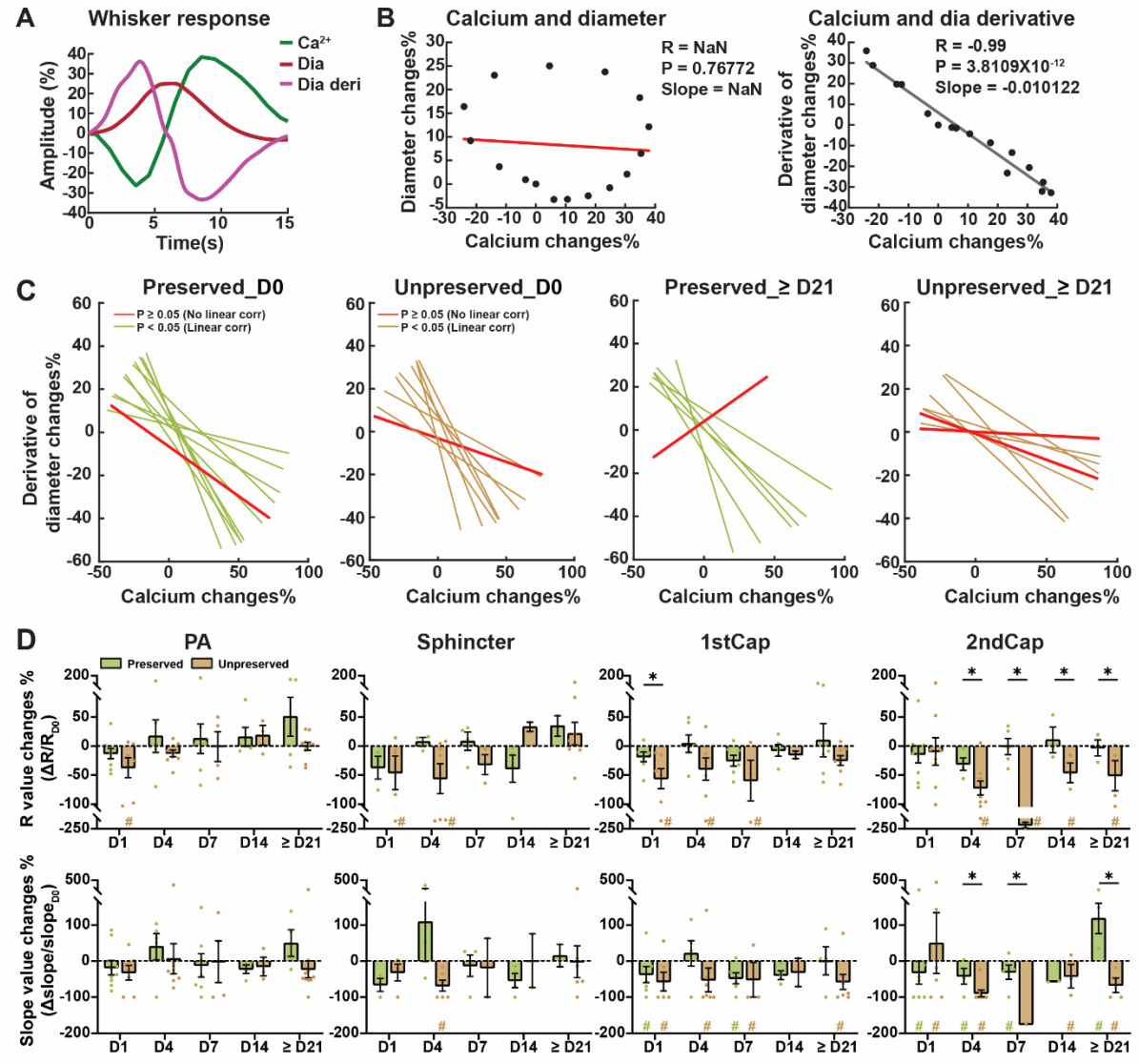
A
Whisker response
Ca2+
Dia
Dia deri
Amplitude (%)
Time(s)
B
Calcium and diameter
R = NaN
P = 0.76772
Slope = NaN
Diameter changes%
Calcium changes%
Calcium and dia derivative
R = -0.99
P = 3.8109X10-12
Slope = -0.010122
Derivative of diameter changes%
Calcium changes%
C
Preserved_D0
Unpreserved_D0
Preserved_≥ D21
Unpreserved_≥ D21
P ≥ 0.05 (No linear corr)
P < 0.05 (Linear corr)
Derivative of diameter changes%
Calcium changes%
D
PA
Sphincter
1stCap
2ndCap
Preserved
Unpreserved
R value changes % (ΔR/R0)
Slope value changes % (Δslope/slope0)
D1
D4
D7
D14
≥ D21

Figure6

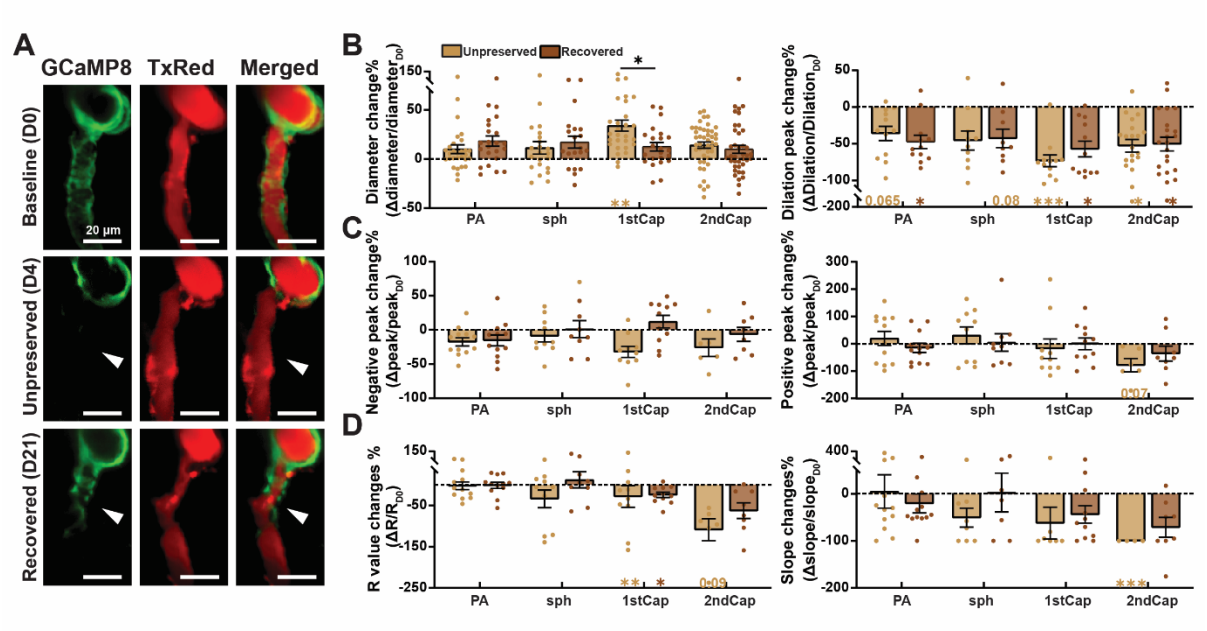
A
GCaMP8
TxRed
Merged
Baseline (D0)
Unpreserved (D4)
Recovered (D21)
20 μm
B
Unpreserved
Recovered
Diameter change%
(Δdiameter/diameter$_{D0}$)
Dilation peak change%
(ΔDilation/Dilation$_{D0}$)
C
Negative peak change%
(Δpeak/peak$_{D0}$)
Positive peak change%
(Δpeak/peak$_{D0}$)
D
R value changes %
(ΔR/R$_{D0}$)
Slope changes%
(Δslope/slope$_{D0}$)
PA
sph
1stCap
2ndCap

Figure7

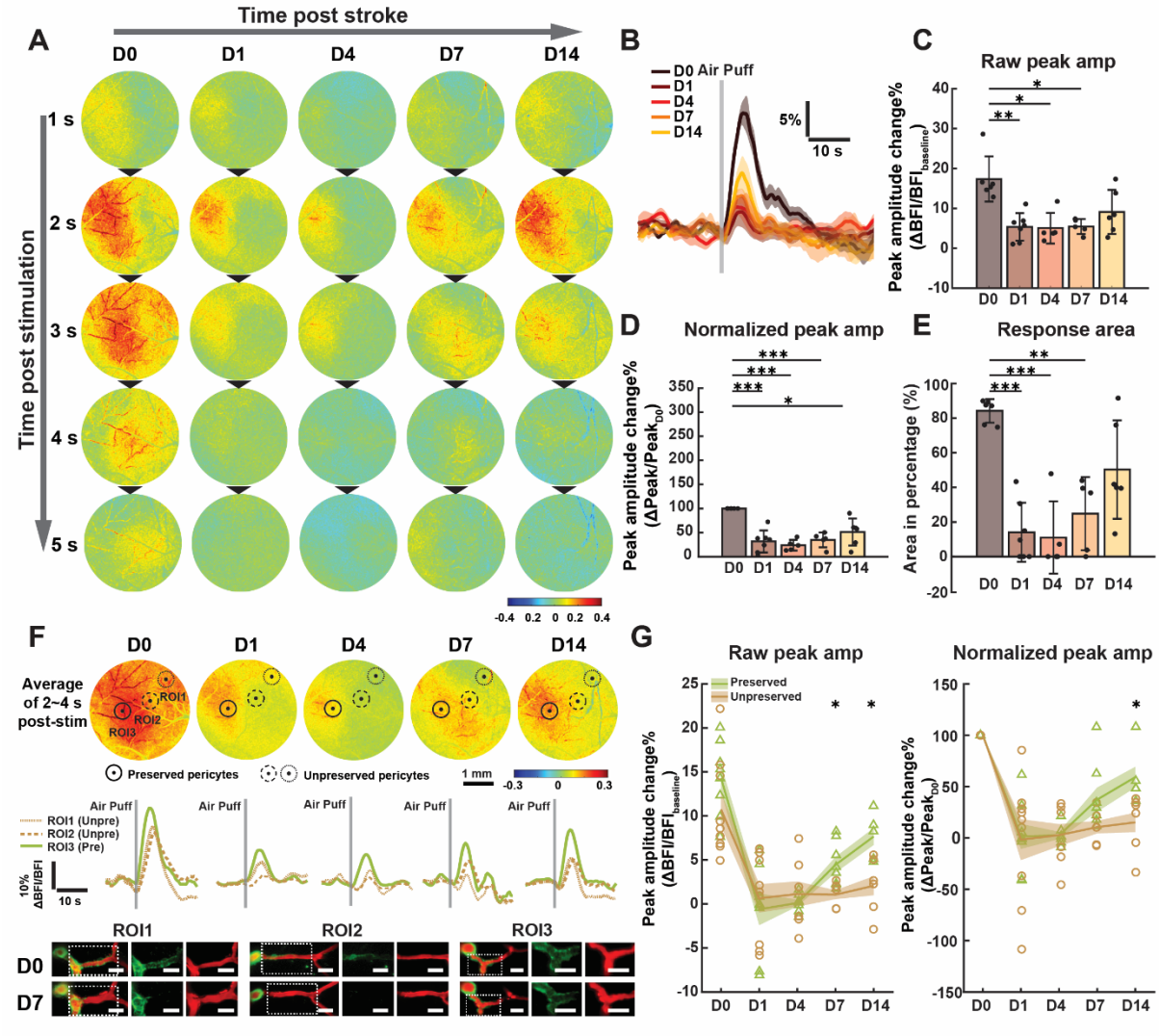
A
Time post stroke
D0
D1
D4
D7
D14
Time post stimulation
1 s
2 s
3 s
4 s
5 s
-0.4 0.2 0 0.2 0.4
B
D0 Air Puff
D1
D4
D7
D14
5%
10 s
C
Raw peak amp
Peak amplitude change%
(ΔBFI/BFI baseline)
D
Normalized peak amp
Peak amplitude change%
(ΔPeak/Peak D0)
E
Response area
Area in percentage (%)
F
Average
of 2~4 s
post-stim
ROI1
ROI2
ROI3
Preserved pericytes
Unpreserved pericytes
1 mm
-0.3 0 0.3
Air Puff
ROI1 (Unpre)
ROI2 (Unpre)
ROI3 (Pre)
10%
ΔBFI/BFI
10 s
G
Raw peak amp
Normalized peak amp
Preserved
Unpreserved